The Thesis Committee for Guillaume Jack Nicolas Noiseau
Certifies that this is the approved version of the following thesis:

Film deposition and mechanical properties of silver produced by impaction of nanoparticles

APPROVED BY
SUPERVISING COMMITTEE:

Supervisor:

Desiderio Kovar

Michael F. Becker

Film deposition and mechanical properties of silver produced by impaction of nanoparticles

by

Guillaume Jack Nicolas Noiseau

Thesis

Presented to the Faculty of the Graduate School of

The University of Texas at Austin

in Partial Fulfillment

of the Requirements

for the Degree of

Master of Science in Engineering

The University of Texas at Austin

December 2012

Acknowledgements

First and foremost I am very grateful to my supervisor, Dr Desiderio Kovar for making my experience at the University of Texas in Materials Science and Engineering possible. His exceptional guidance, precious advice and knowledge of the field were invaluable for the completion of my work. I would also like to thank the other faculty members of the LAMA group, Dr Michael F. Becker and John Keto, for their help and sharing their knowledge and experience. I would like to thank members of the MSE staff, Clarissa Pena, Joan Hadden and Rebecca Christian for their help upon my arrival and during the preparation of my Master. Among my colleagues, Romain Fleury deserves special thanks for showing me the ropes of the LAMA process, and for spending time with me to make sure my first experiments worked. Finally, I would like to thank all my colleagues and friends, Kris Gleason, Michael Gammage, Manuj Nahar, Claire Davis, Jean-Gil Gutierrez, Blake Perez, and Alex Scheuermann.

Abstract

Film deposition and mechanical properties of silver produced by impaction of nanoparticles

Guillaume Jack Nicolas Noiseau, MSE

The University of Texas at Austin, 2012

Supervisor: Desiderio Kovar

Nanocrystalline films are promising in various fields such as microelectronics. Low temperature deposition techniques are desirable since they would enable the use of new substrates that are temperature sensitive, leading to a wide range of new applications. This thesis explores nanocrystalline silver film deposition by impacting nanoparticles (NP) onto a substrate, a technique that enables low process temperatures. This work aims at better understanding the physical parameters governing the sticking probability of NP upon impaction. To achieve this, various substrate materials have been used (metallic and non metallic) and the influence of the impacted substrate temperature has been studied, among other experiments. These parameters showed a significant influence on the collection efficiency of NPs. These experimental results are analyzed in light of published computer simulations studies predicting the behavior of impacting NP to deposit nanostructured films. Secondly, a study of the mechanical properties of the

deposited films has been attempted. Compression tests have been carried out varying the applied load, loading time and process temperature. The produced films are nanocrystalline and porous (~70% relative density). Densification has been observed even at room temperature, and the goal of this study is to understand which mechanisms cause the densification to occur. The experimental densification data are compared with a model describing the densification of microparticles compacts by hot pressing that has been adapted to nanocrystalline silver, and the mechanisms leading to densification are discussed.

Table of Contents

List of Tables

List of Figures

1. Introduction

1.1 Applications of thin films

Nanomaterials exhibit at least one dimension that is the scale of a nanometer. The focus of this thesis is a material in which the building blocks that make up the material – the grains– are themselves nanometric but the devices from which the materials are made are micron- or even millimeter-scale. Nanomaterials are increasingly popular among researchers and industries, who try to understand their unique properties and to take advantage of these to develop new processing techniques or applications. One area where there has been active research is the area of conductive patterned films. Applications for such films include low temperature solutions for packaging of microelectromechanical systems (MEMS) [21] [26].

Conventional approaches for producing conductive films utilize a mask to pattern a paste that contains metallic microparticles (MPs). To obtain a continuous material and thus a high electrical and thermal conductivity, those particles are subsequently heated at relatively high temperature (typically 75% of the melting temperature [27]). This process of forming continuous, dense materials from particles is called sintering and requires high temperatures because it is governed by diffusion of atoms through the microstructure.

MEMS packaging is designed to protect the MEMS elements and interface them with the exterior environment. A common technique used for packaging is metallic layer wafer bonding, where a ring seal pattern is deposited and subsequently bonded to a wafer

to create a hermetic seal [21]. Reducing the processing temperatures required to produce highly conductive packaging is desirable because it would enable the use of lower cost substrates and enable new devices that are too temperature sensitive to be produced using current high temperature packaging techniques.

One strategy to reduce the processing temperature is to reduce the size of particles down to the nanometric scale. Sintering can be enhanced as the particles size is reduced because of the following: (1) the diffusion distances are much shorter, (2) the mass to be transported for sintering is much smaller than in the case of microparticles and (3) the curvature of the nanoparticles is much sharper, leading to larger chemical potential gradients [27]. Nanoparticles can thus be sintered or wafer bonded at lower temperature than bigger particles.

In summary, nanomaterials are promising for applications in MEMS packaging, since they potentially allow low processing temperature that lead to a wide range of new applications. To utilize these materials, both the physics of the film deposition, as well as the mechanical behavior of the resulting films needs to be better understood, since they are of great importance in the targeted applications.

1.2 The Laser Ablation of Microparticle Aerosol Process

The laser ablation of microparticle aerosol (LAMA) process is used to produce the films studied in this work. The process consists of two main steps: First, the

production of a nanoparticle (NP) aerosol from microparticles (MPs). Then, the created NP aerosol is accelerated and NPs are impacted onto a substrate. The impacting particles have sufficient energy to cause the particles to stick on the substrate and build up nanostructured films. These three aspects are discussed in the subsections that follow and a fourth subsection highlights the advantages of the LAMA process over other film formation methods.

Figure 1.1: Overview of the LAMA process used to produce silver films

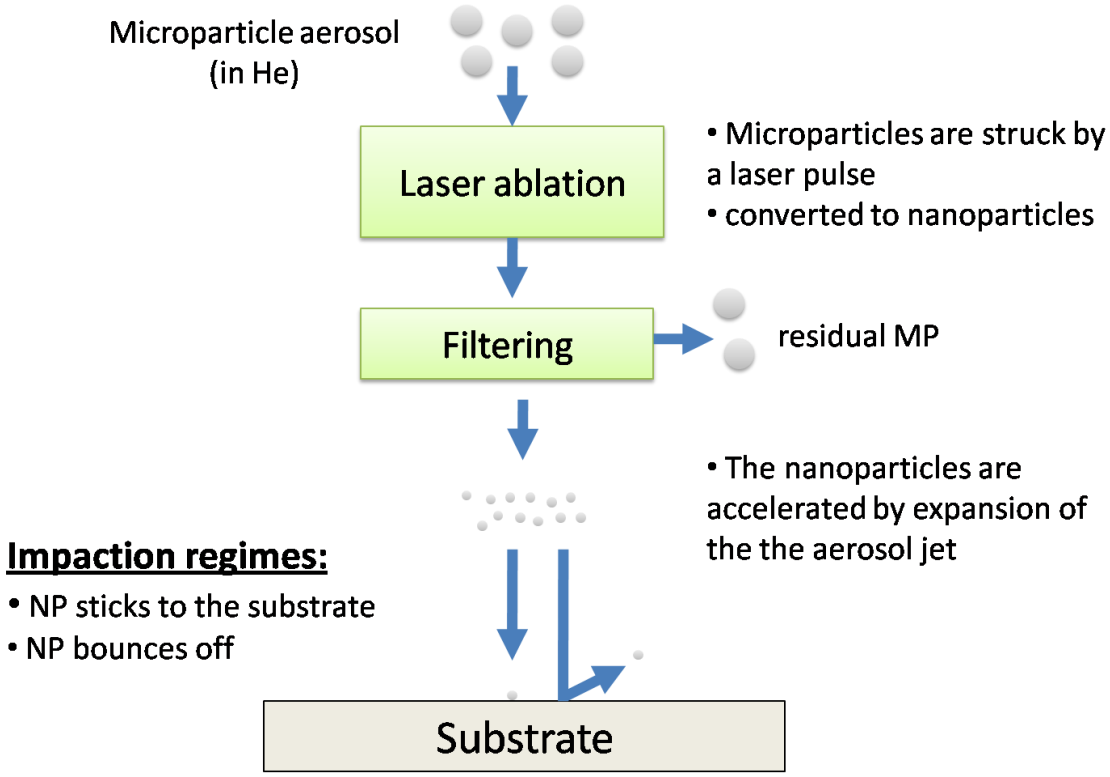

1.2.1 Laser ablation of microparticles

The physics of nanoparticles formation when microparticles are illuminated by a laser pulse are described previously [22]. Two regimes of NPs formation are possible depending on the laser fluence (energy per unit area): At a low fluence, the laser energy is uniformly absorbed by the MP, which sublimates. NPs formation results by subsequent condensation of the vapor but particles produced from this mechanism tend to have a wide size distribution [29]. A second mechanism for NP formation occurs if the fluence exceeds the threshold for plasma breakdown, and a shockwave is produced that travels through the MP. NPs form in the rarefaction region [22]. The shockwave-driven regime results in finer particles with a narrower size distribution, and has therefore been selected for this work.

Figure 1.2: Formation of nanoparticles following laser ablation of a microparticle

Reprinted from [1]

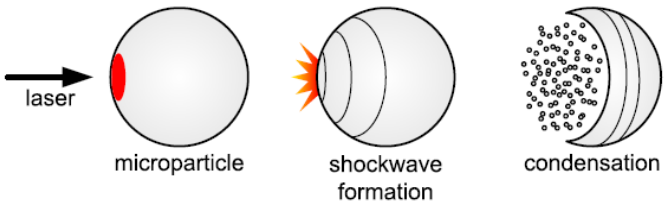

Some relevant features of the nanoparticles produced by LAMA are that they are free of any organic surfactant, and, if they are small enough, they do not contain dislocations. Indeed, it has been shown that dislocations are unstable in nanoscale particles, as any dislocation that would nucleate within the NP would instantaneously migrate towards its surface [23]. Figure 1.3 shows a TEM picture of NPs produced by

LAMA with helium as a carrier gas, similar to the NPs produced in this work. The dark object in the lower left of the micrograph is a copper grid that is supporting the lighter grey carbon support film. The NPs are deposited on the carbon support film.

Figure 1.3: Silver nanoparticles produced by LAMA. Reprinted from [10]

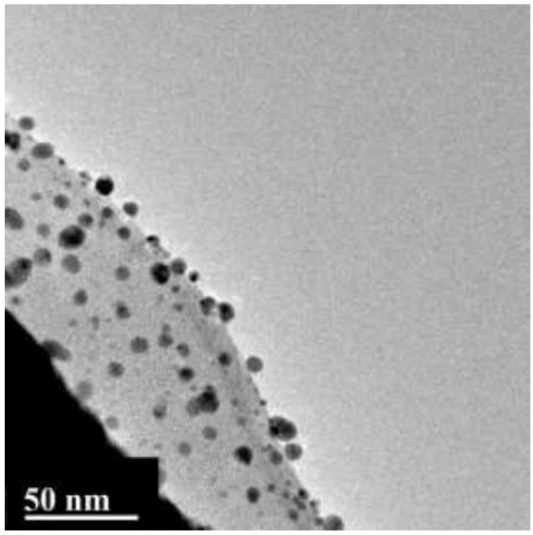

1.2.2 Acceleration of nanoparticles in an aerosol jet

After the conversion of the MP aerosol into a NP aerosol, the NPs are accelerated by expansion of the carrier gas through a nozzle using a pressure differential. Huang *et al.* [3] studied the gas dynamics during acceleration of the flow and developed a theoretical model based on fluid mechanics to predict the speed reached by the carrier gas and by the NPs. The qualitative and quantitative results of this model are of great importance for the understanding of the impact process, which is further discussed in Chapter 4. Some of the most relevant results are reprinted in Figure 1.4. Figure 1.4a shows the maximum velocity reached by the expanding aerosol gas and Figure 1.4b

shows that the velocity of a typical 5 nm particle is predicted to be over 1000 m/s upon impaction onto a substrate.

Figure 1.4: a) Gas velocity (He) when accelerated by a pressure differential through a flat-plate nozzle. d is the nozzle diameter, z the distance from the nozzle. b) NP impaction velocity vs. particle diameter. Reprinted from [3]

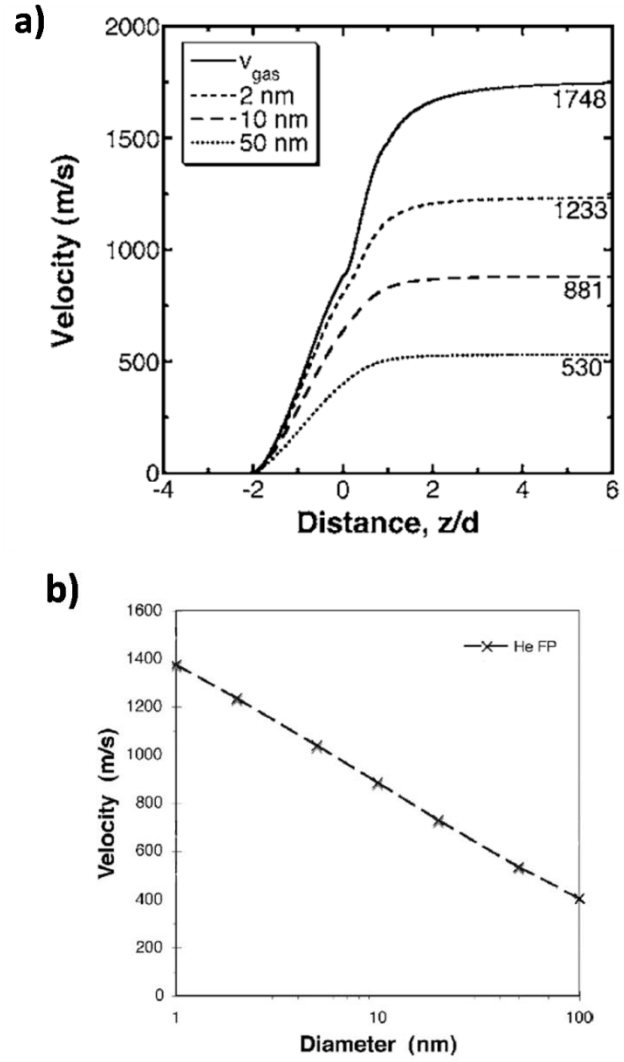

1.2.3 Physics of nanoparticle impaction

The behavior of NPs impacting on a surface to create films has been actively investigated, in particular using molecular dynamics (MD) computer simulations [5]. The particle kinetic energy and size have been identified as the two governing factors. The MD simulations have shown that when a particle impacts a surface, several regimes are possible. The regimes relevant for this work are (1) no deposition (or NP bounce-off) at the lowest energies, (2) deposition in a non-epitaxial configuration, and, (3) deposition in an epitaxial configuration, where atomic planes of the NP align with those of the target surface. Epitaxial deposition occurs for small NP or when the kinetic energy is high; it is hypothesized that the kinetic energy in this regime is sufficient to cause heating of the NP above the melting point of the particle.

Figure 1.5: MD computer simulations of NP impact. a) Low energy, non epitaxial deposition. Only the lowest atomic planes are aligned with those of the impaction substrate. b) Epitaxial deposition (both taken from [5])

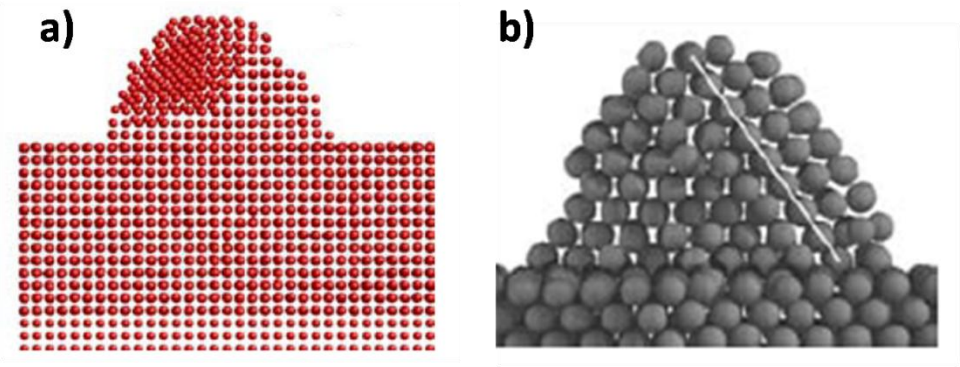

1.2.4 Advantages of the LAMA Process

The LAMA process presents several advantages for the production of nanomaterials. First, virtually any inorganic material under the form of MPs can be used as a starting material. The production of nanoparticles is thus independent of any chemical route, which makes the process exceptionally flexible. Secondly, no residual organic layer is present at the surface of the produced NPs; the films produced by LAMA thus do not require any post-deposition annealing process to remove these residual organics. Lower temperature processing is thus possible.

1.3 Previous results on nanostructured thin films produced by LAMA

The LAMA system to produce nanoparticles and nanostructured films has been developed over the past decade. Many of its aspects have been investigated, such as the supersonic acceleration of nanoparticles within an expanding background gas and the effect of background gas on the size and impacting energy of NPs (Huang *et al.* [3]), the influence of the feedstock aerosol density on the agglomeration dynamics of NPs (Gleason *et al.* [1]). This system has also been tested with various starting feedstock materials, such as metals or ceramics (Gallardo *et al.* [4]). Finally, low temperature sintering, grain growth and conductivity of nanoparticulate silver lines have been studied by Albert [9], Huang [3] and Nahar [10].

1.4 Scope of this work and motivation

In this thesis, I report on the processing and characterization of nanoparticulate silver lines and films. After a brief presentation of the experimental setups and procedures in Chapter 2, I present in Chapter 3 the general morphology of the silver lines that have been produced. Chapter 4 reports on a parametric study carried out to better understand the impaction process of supersonically accelerated silver NPs. Chapter 5 focuses on the mechanical behavior of nanostructured silver lines. Compression experiments have been carried out varying the applied load, the loading time and process temperature. In particular, densification of nanostructured silver has been observed and the mechanisms leading to the deformation are discussed.

2. Experimental equipment and procedures

In this chapter, the equipment to produce an aerosol of nanoparticles is first described. Secondly, the setup to direct write films is presented. Thirdly, the setup to test the mechanical behavior of nanostructured silver films is presented. Finally, the various methods used to characterize the lines and films produced for this work are described.

2.1 Production of a NP aerosol

The LAMA setup to produce an aerosol of NPs is presented in Fig. 2.1. In summary, the LAMA process converts an aerosol of MPs into an aerosol of NPs by generating a shockwave within the MPs using a pulsed excimer laser. An aerosol of MPs is first generated and directed to the ablation chamber (section 2.1.1). The laser beam is directed and focused to the ablation zone using a combination of two lenses (section 2.1.3) to convert the aerosol of MPs to an aerosol of NPs. The aerosol is then directed through a virtual impactor to eliminate any residual MPs or larger agglomerated NPs (section 1.1.4). The resulting aerosol of NPs is finally accelerated to high velocities (section 2.2.1) and directed onto a translating substrate to write patterned films (2.2.2 and 2.2.3).

Figure 2.1: LAMA Setup for the production of a NP aerosol

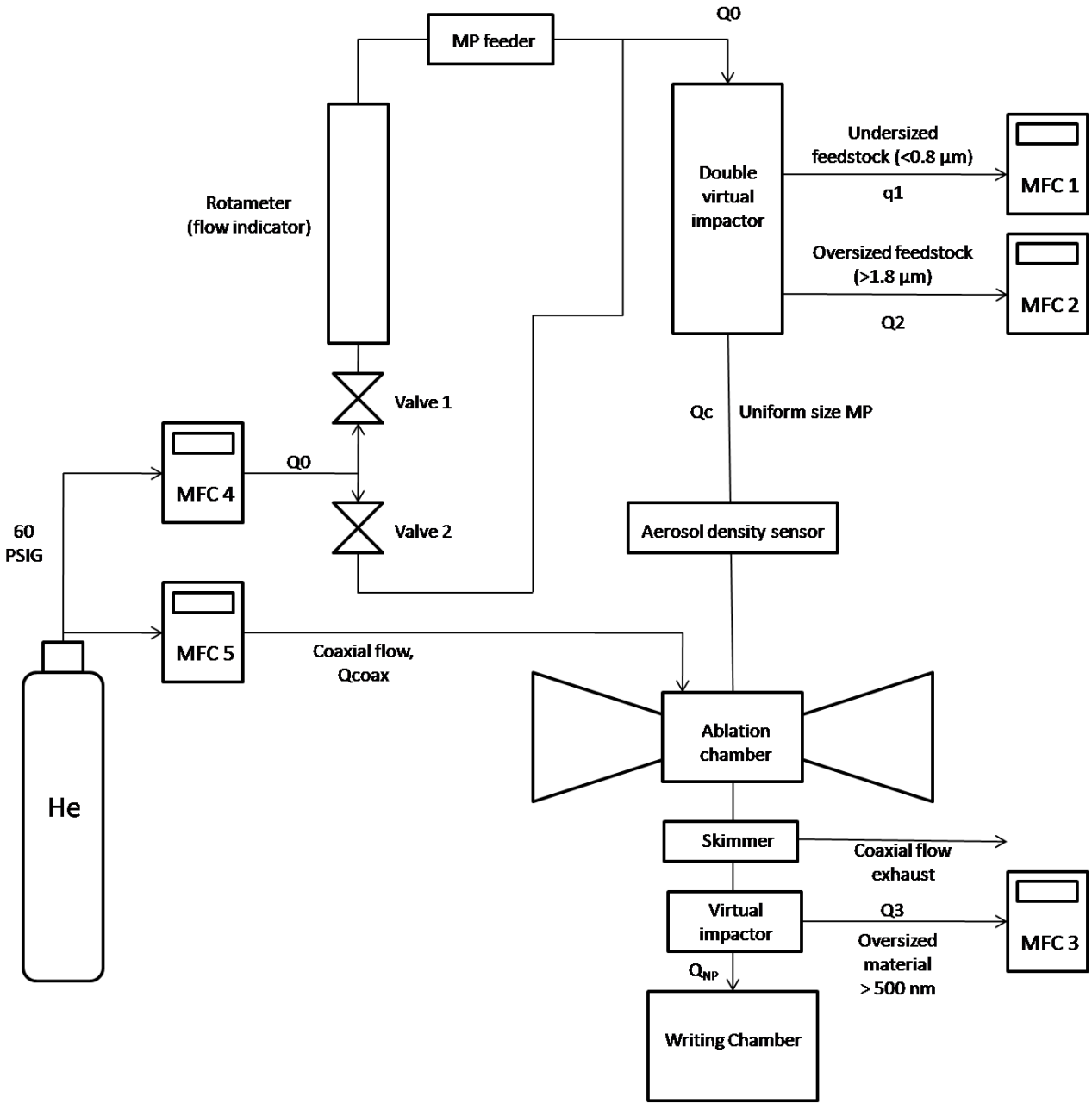

Table 2.1: Values of the gas flows used in the LAMA process

	Flow rate sccm	Description
Q_0	2717	Input flow
q_1	217	Minor flow 1 (1^{st} step of double virtual impactor)
Q_2	2300	Major flow 2 (2^{nd} step of double virtual impactor)
Q_c	200	Center flow (MP aerosol undergoing ablation)
Q_{coax}	5921	Coaxial or outer flow
Q_3	192	Virtual impactor flow (Oversize material downstream ablation > 500 nm)
Q_{NP}	2209	NP flow (supersonically accelerated NP aerosol)

2.1.1 Aerosol powder feeder

The first step in the LAMA process is to create an aerosol of MPs. To do so, helium gas is passed through a MP powder bed. The input flow (Q_0) of helium is controlled by a mass flow controller. Since the MPs feedstock contains agglomerated MPs along with individual MPs, a preliminary step is necessary remove the agglomerates. A double virtual impactor setup has been developed by Gleason *et al.* for this purpose, and its design is discussed in [1]. The resulting aerosol (Q_c) only contains MPs with a narrow size range of 0.8-1.8 µm. The two flows q_1 and Q_2 used for the aerodynamic size selection in the virtual impactor are controlled with mass flow controllers as well.

2.1.2 Control and monitoring of the aerosol density

An aerosol density detector (whose design is also discussed in [1]) is used to monitor the MP aerosol feed rate in real time. In short, the operating principles of the detector are as follows: the scattering of a He-Ne laser beam by the MPs flowing in the

aerosol is measured by a sensor. The sensor output is then correlated to a given powder feed rate (given in mg/hr) using a prior calibration. The feed rate is then monitored in real time on a graphic user interface using Labview® (National Instruments Inc., Austin, TX). In this study, a powder feed rate of 10 mg/hr is used.

The aerosol density is adjusted manually by adjusting both the valves V1 and V2 (see Figure 2.1). To increase the aerosol density, the helium flow through the powder feeder is increased (by slightly opening V1 and/or closing V2). To decrease the aerosol density, the flow through the powder feeder is reduced by slightly closing V1 and/or opening V2. This configuration enables a constant main flow (Q_0).

2.1.3 Optical system and laser ablation chamber

A KrF excimer laser (λ = 248 nm) is used at its maximum repetition rate of 200 Hz for the laser ablation. Two cylindrical lenses of focal lengths f1 = 110 cm and f2 = 14 cm are used to focus the beam respectively horizontally and vertically (see Figure 2.2). For this work, the laser beam energy was set at 250 mJ and the beam area at the ablation zone was measured to be 0.08 cm^2, resulting in a fluence of 3.1 J/cm^2, which is above the breakdown threshold for Ag MPs (0.8 J/cm^2 [22]).

Figure 2.2: Optical setup for focusing the laser beam at the ablation zone

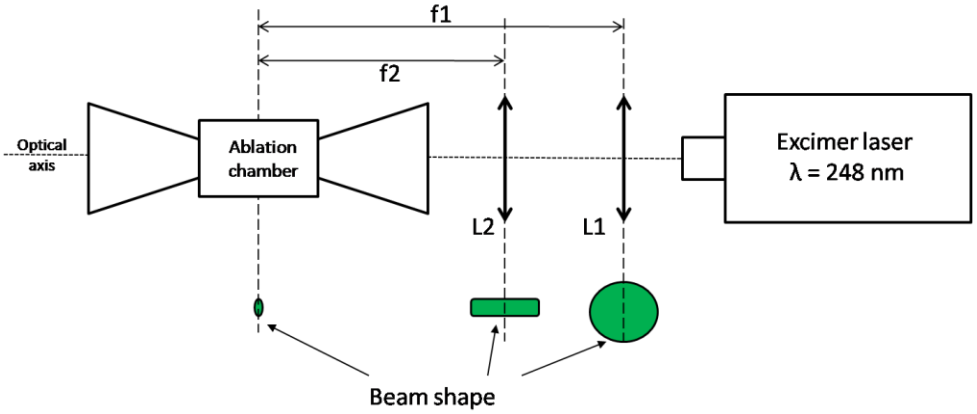

The ablation zone lies at the center of the laser ablation cell (see Figure 2.2). The MP aerosol is circulated through the ablation zone via a nozzle. The gas velocity of the MP aerosol (center flow, Q_c) is adjusted so that MP are ablated by the laser only once. In addition, to ensure that the aerosol flow remains laminar in the ablation zone, a buffer gas with the same linear velocity as the aerosol surrounds the MP aerosol.

Equation (2.1) is used to determine the flow rate for the center flow, which depends on the area of the feed nozzle, A_{center}, the frequency of the laser, f, and the height of the ablation zone, h.

(2.1) $$Q_c = A_{center} \cdot f \cdot h$$

The flow rate for the coaxial flow, Q_{coax}, to maintain laminar flow, is given by:

(2.2) $$Q_{coax} = Q_{center} . (A_{outer}/A_{center} - 1)$$

where A_{outer} is the area of the outer flow and other parameters are defined above.

2.1.4 NP size selection using a virtual impactor

Figure 2.3: Ablation chamber, skimmer and virtual impactor assembly (taken from [1])

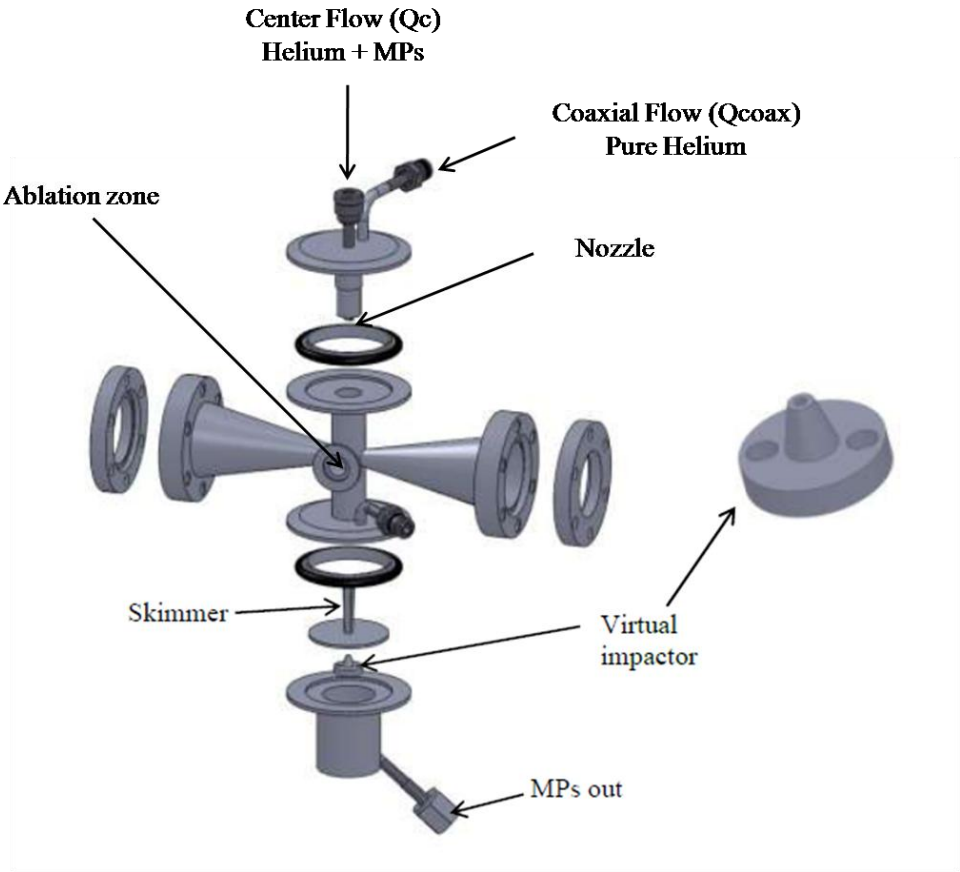

Downstream of the ablation zone, the center flow Q_c is collected into a skimmer and the coaxial flow Q_{coax} is evacuated to a fume hood. The center flow contains of mix of individual NPs and NPs that agglomerated following the ablation process. To remove the agglomerates, a virtual impactor is used. It operates as an aerodynamic size selector, sorting out the oversize material that stays in the inner streamlines of the aerosol [28]. The smaller particles (individual NPs and small NPs agglomerates) contained in the outer streamlines are directed into the direct write chamber. The virtual impactor used in this work has a cutoff size of 500 nm.

2.2 Direct writing of nanoparticulate films

2.2.1 Acceleration of NPs

After ablation and aerodynamic size selection, the resulting aerosol contains NPs that have a mean size of approximately 5 nm and a narrow size distribution, as has been shown in previous studies [22].

Figure 2.4: Direct writing chamber setup

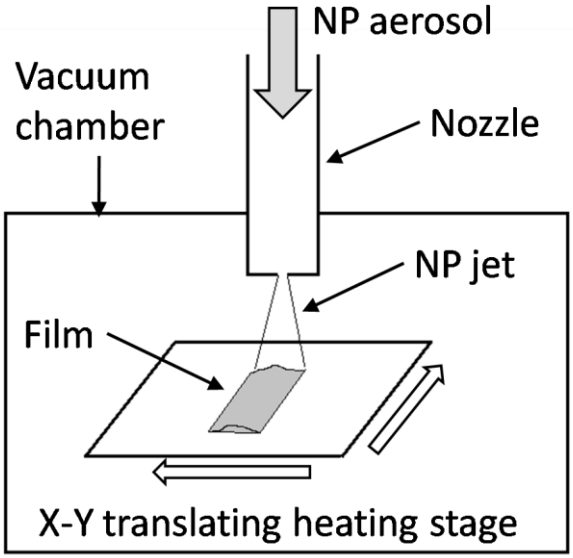

The NPs aerosol is subsequently accelerated though a flat-plate nozzle with a 250 μm orifice via a pressure differential (see Figure 2.4). The pressure upstream of the nozzle is maintained at atmospheric pressure and the direct-write chamber (downstream the nozzle) is pumped to 200 mTorr. Previous calculations have shown that the Ag NPs in this size range have a velocity of approximately 1000 m/s at impaction [3].

2.2.2 Computer-controlled translating stage

A computer-controlled stage placed below the nozzle enables writing of patterned films. The translation speed and number of passes of the stage below the nozzle allows the control of the thickness of the films. Further details on the writing parameters are given in Chapter 3.

Figure 2.5: X-Y stage control

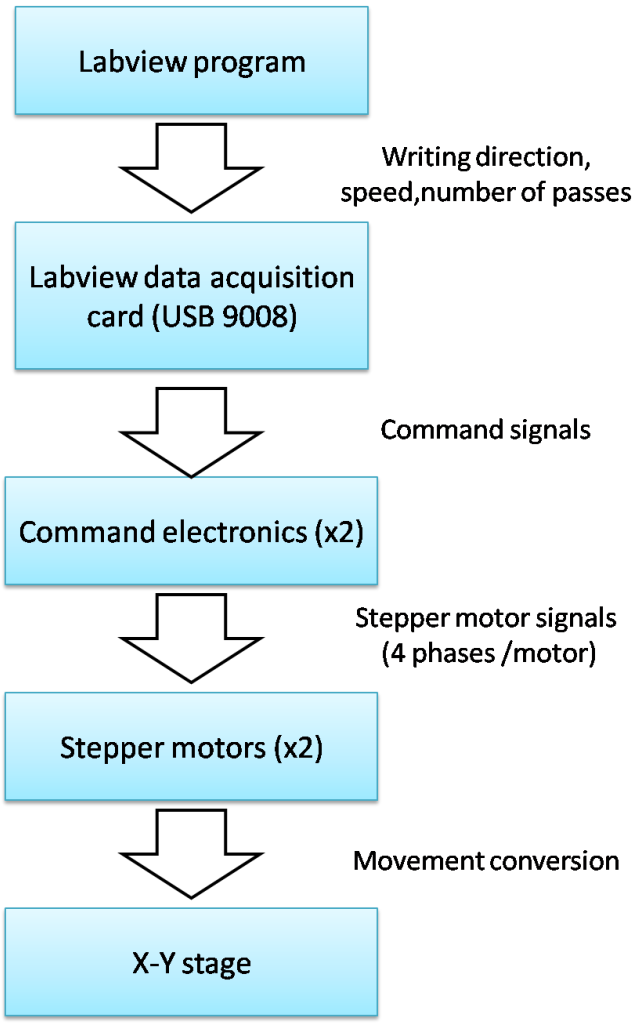

The translation both in X and Y directions relies on stepper motors. A Labview VI(virtual instrument) is used to control the motors' speed and direction. Appropriate signals for the stepper motor phases are provided by electronic circuits, which are themselves controlled by a Labview data acquisition device (USB 9008, National Instruments Inc., Austin, TX) and Labview VI (see Figure 2.5).

2.2.3 Heating stage

To study the influence of substrate temperature on film formation and the morphology of the films, a temperature-controlled substrate holder has been implemented on the translating stage. A cylindrical piece of steel or substrate holder (1" diameter, 1.5" height) has been machined into which a 250W cartridge heater (Model CSH-101100/120V, Omega Engineering, Stamford, CT) and a type K thermocouple are inserted. Both are connected to a PID controller (Model CN9000A, Omega Engineering, Stamford, CT) that enables the control of the temperature. The maximum temperature of the stage is about 400°C with a precision of ± 1°C.

2.3 Temperature-controlled mechanical testing setup

To study the mechanical behavior of nanostructured lines and films, compression tests have been carried out, where both temperature and pressure are monitored and controlled. A test frame (Sintech 2/G, MTS®, Eden Prairie, MN) with a 10kN load cell (Hitec®,Littleton,MA) are used to control the applied pressure. Both the upper and lower punches used for compression were configured with temperature controllers as described in 2.2.3.

To prevent the loadcell from overheating (which could lead to false readings or even damage), a cooling system using circulating refrigerated water (Model A82, Haake, Karlsruhe, Germany) was used to cool the threaded rod connecting the punch to the load cell. This cooling system was set to cool down the rod at 1°C, and this temperature was also monitored.

Figure 2.6: Temperature-controlled compression setup

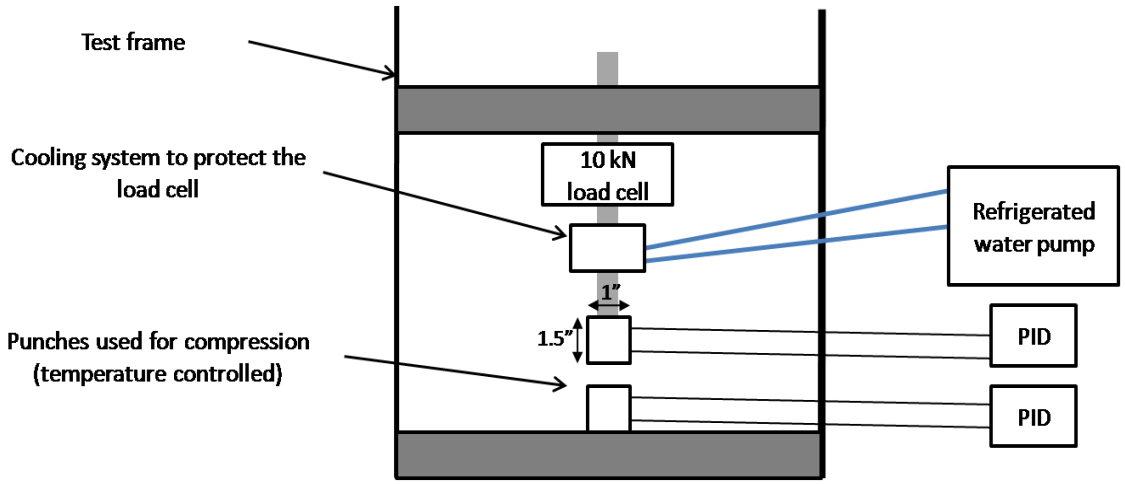

2.4 Characterization of the films

2.4.1 Optical profilometry

An optical profilometer (Model Zeta-20, Zeta instruments, San Jose, CA) is used to capture images of the specimen surface and profiles of the produced lines/films. The objective lens is first adjusted to focus on the highest point on surface. It is then adjusted to focus on the lowest point. The profilometer automatically scans the surface between these two extremes values. For each increment in height of the lens (typically there 200

increments), the profilometer determines which areas of the sample are in focus and thus determines their height relative to the lowest position. Finally, included software reconstructs a 3D image of the surface. The highest magnification lens that is available with the profilometer (100×) is used to maximize precision. The profilometer allows the measurement of the thickness of the films with a precision of at least 0.5 µm.

2.4.2 Electron microscopy

A scanning electron microscope (JSM-5610, JEOL, Ltd. Tokyo, Japan) has been used to acquire plan view micrographs of the silver films (secondary electron signal).

2.4.3 Direct density measurements

The density of nanostructured silver is estimated by weighing the substrate before and after deposition of a 4 mm × 4 mm square film. The deposition of this relatively large area enables sufficient mass to be deposited so that it can be measured with a precision scale (± 0.00005 g). The volume is determined using a feature of a Zeta profilometer that uses the acquired 3D surface profile and integrates the height along the length of the line to obtain the corresponding volume. The density has simply been determined by dividing the volume by the mass.

2.5 Procedure for coating silicon substrates with an Au/Pd layer

An Ar-sputterer (Pelco SC-3, Ted Pella, Redding, CA) primarily used for SEM sample preparation has been used to coat silicon substrates with a thin layer of Au/Pd, to study the influence of this metallization. The parameters were set as follows: current: 15 mA, sputtering time: 30 s. Although thickness was not determined, typical coating thicknesses for sputtering at similar conditions result in a coating that is about 2 nm thick [30].

3. Direct writing of nanostructured thin films

This chapter presents the general characteristics of the lines and films produced with the LAMA/direct writing setups, and shows how the writing parameters influence their morphology.

3.1 Experimental parameters

3.1.1 Aerosol feed rate

The aerosol feed density can be controlled precisely from 5-50 mg/hr with the current system. The advantage of using a higher feed rate is that more material is deposited. However, at higher feed rates, more MPs are fed in the ablation zone, resulting in a higher density of NPs formed in and downstream of the ablation zone, and this results in an increased probability of forming agglomerates. Thus, even if high deposition rates are desirable to maximize the efficiency of the process, it is preferable to work at feed rates at or below 10 mg/hr to minimize the amount of agglomerated NPs and unablated feedstock MPs. Also, during the ablation, the probability increases that some MPs are shadowed by other MPs, and thus are not struckby the laser beam. This leads to residual unablated feedstock downstream of the ablation. Such NP agglomerates and unagglomerated MPs are visible on films written at high feed rates, despite the post ablation aerodynamic size selection step (see Figure3.1), because it is possible to overwhelm the virtual impactor if a high density of agglomerates are fed.

Figure 3.1: SEM picture (plan view) of a line written with a feed rate of 15 mg/ hr. White particles are agglomerates.

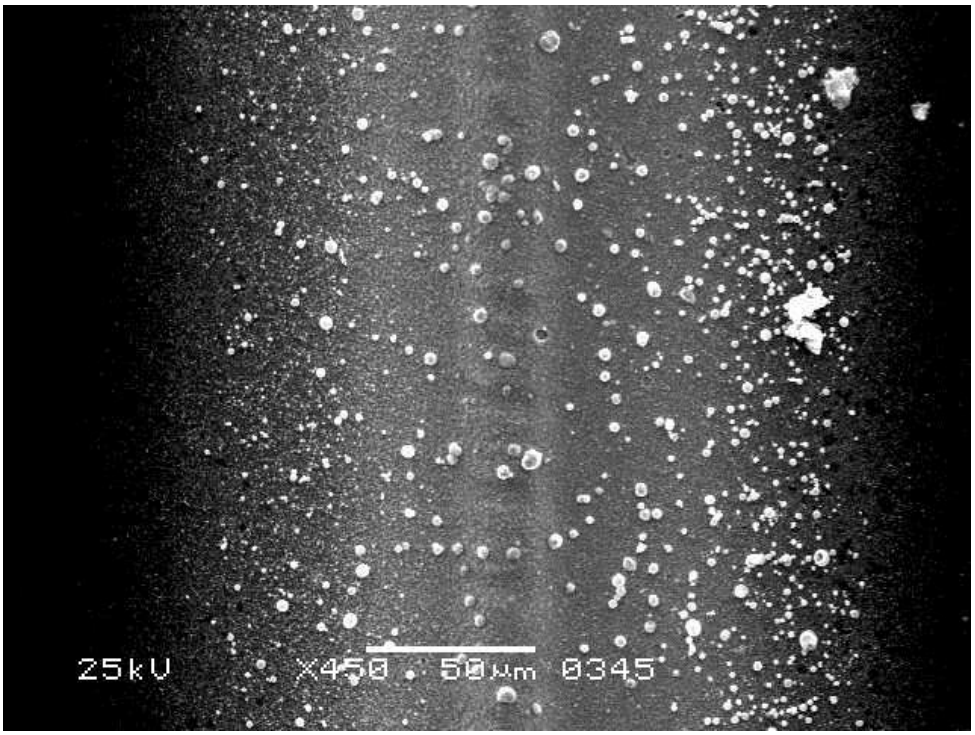

3.1.2 Writing parameters

The method and speed that the substrate holder is translated below the nozzle influences the morphology of the films. If the substrate holder is rastered more slowly, the film thickness increases, as shown in Figure 3.2. Alternatively, the film thickness can also be increased by traversing back and forth several times over the same region of the substrate. It has been observed that increasing the number of passes increases the uniformity of the films, since it results in averaging of fluctuations in the feed rate. Films written with 30 passes are very uniform in height, with a typical variation in height of ± 1µm (or 10% of the total height). Typical lines produced for this work are several

centimeters long, 100-200µm wide and 1-80 µm thick, depending on the translational speed and number of passes.

Figure 3.2: Height of the lines vs. writing velocity for 1, 3 and 10 passes (measurement errors for the line height are less than 0.5µm)

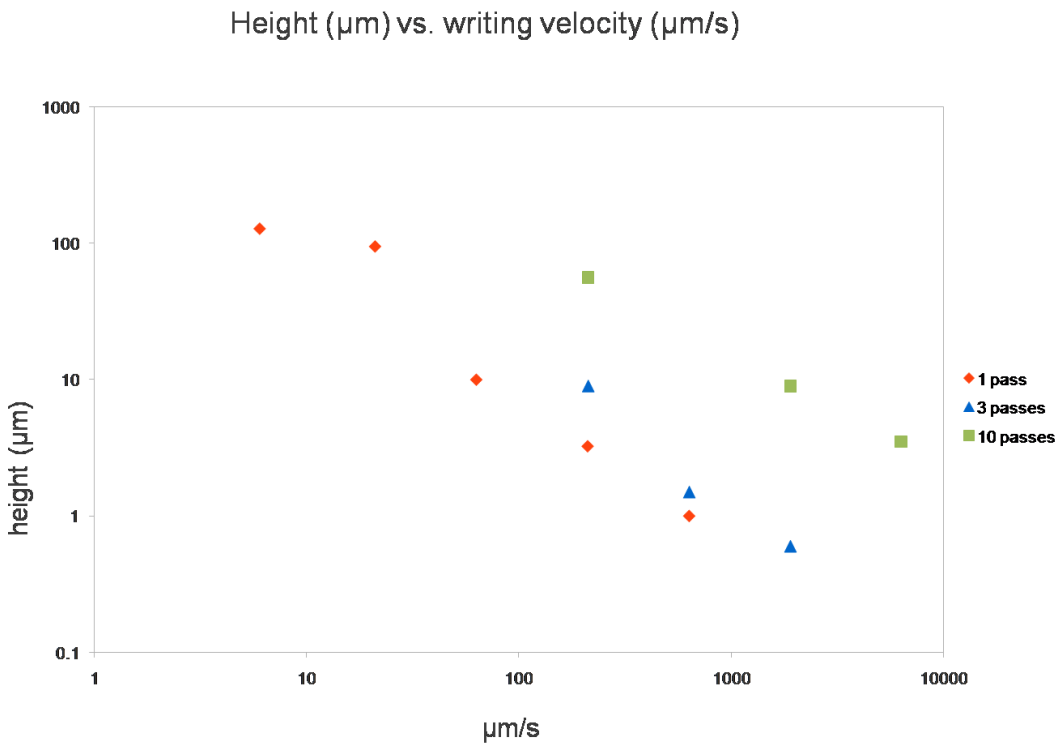

3.2 Morphologiesof typical films

Figures 3.3 and 3.4 show typical lines written at different writing velocities (1.9 mm/s and 6.5 mm/s), all other parameters being equal. Although the line written at 1.9 mm/s is thicker, the line written at 6.5 mm/s is more uniform in height across the whole length of the line.

Figure 3.3: Line written at 1.9 mm/s (30 passes) with a 10 mg/hr feed rate and 1.2 mm nozzle-to-substrate distance. a) Planview b) Oblique view c) Cross-sectional profile obtained with a Zeta© profilometer

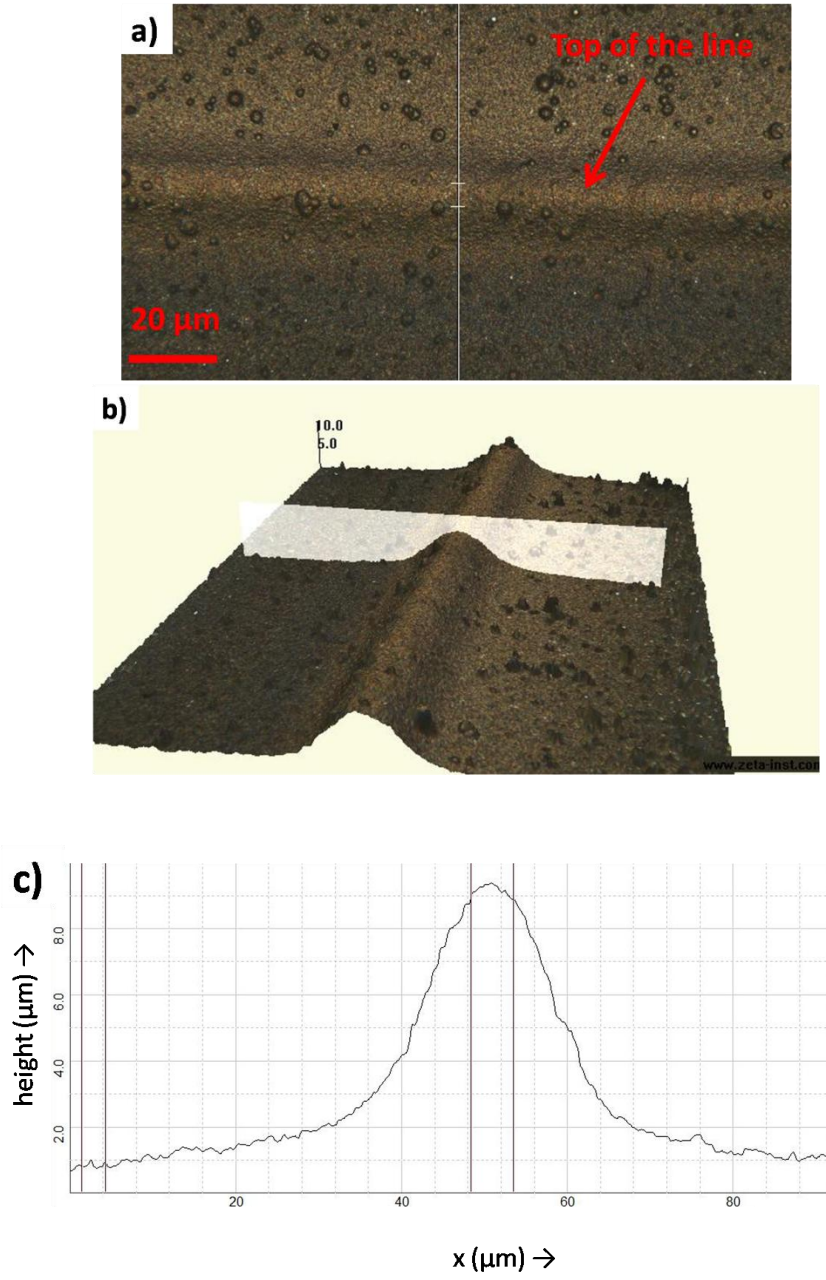

Figure 3.4 Line written at 6.3 mm/s (30 passes) with a feed rate of 10 mg/hr and a nozzle to substrate distance of 1.2 mm. a) Planview b) Oblique view c) Cross-sectional profile obtained with a Zeta© profilometer

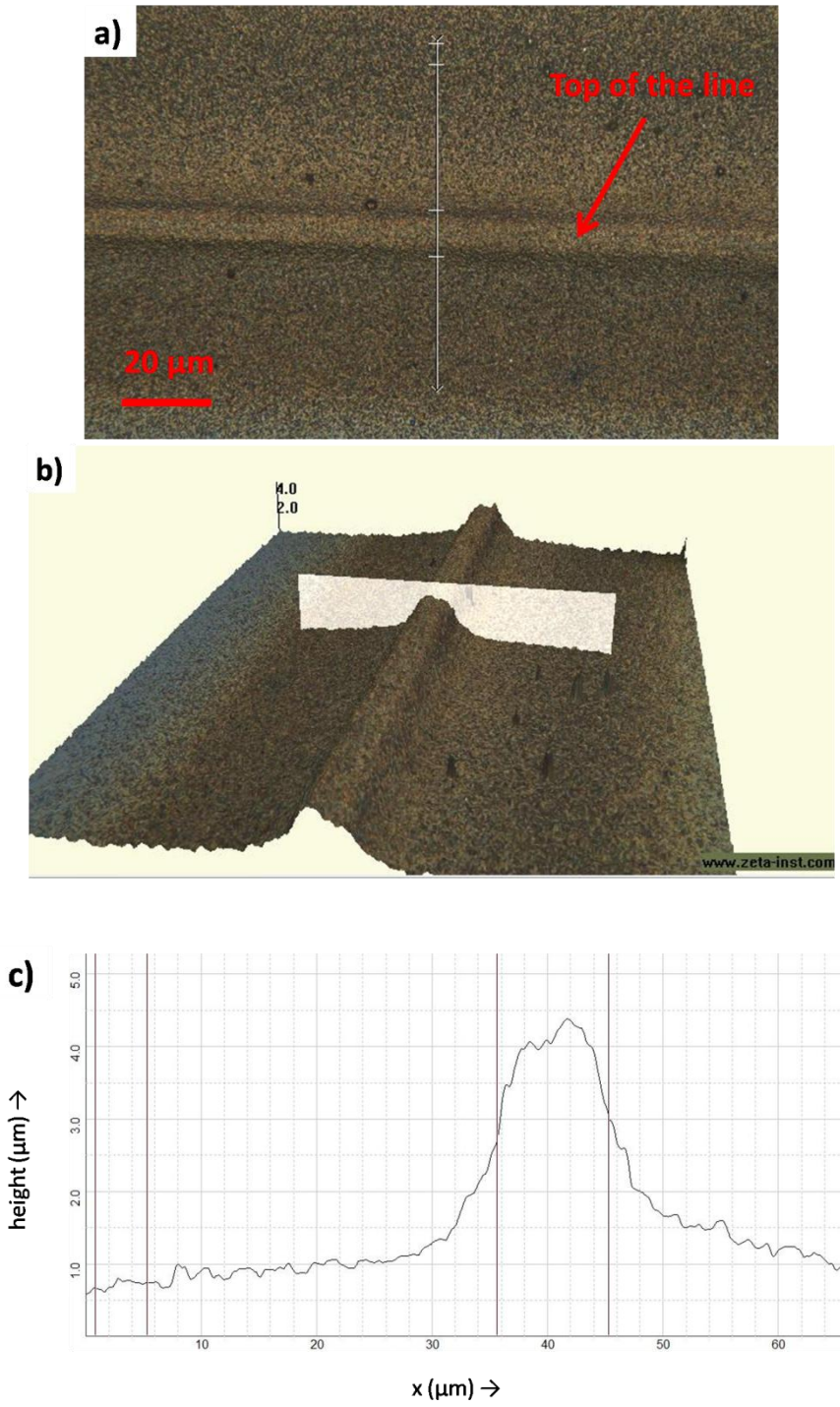

4. Deposition efficiency for supersonically impacted Ag nanoparticles

This chapter explores the deposition efficiency for nanoparticles impacting onto a surface. Many studies based on Molecular Dynamic (MD) computer simulations have been published on this subject [5]-[8] but to our knowledge the influence of substrate temperature and material have not been investigated experimentally. The MD simulations predict that the deposition efficiency depends primarily on the particle size and kinetic energy. We present experimental results where we have measured deposition efficiency as we vary substrate material, substrate temperature, and impaction velocity/angle.

4.1 Background

4.1.1 Acceleration of NPs in an aerosol jet

Previous studies by Huang *et al*. [3] and de la Mora *et al.* [25] investigated how particles are accelerated in an aerosol jet. It has been shown that for a flat plate nozzle with an upstream pressure P_0 and downstream pressure P_1, if the ratio P_0/P_1 is large, a supersonic jet is formed and the flow is choked. The resulting jet then forms a bow shock as its expansion is blocked by the substrate [25].

In this work, a sufficient nozzle-to substrate distance is chosen to allow the gas to reach its maximum velocity, but small enough to prevent the formation of a Mach disk, that occurs when the gas recompresses to a pressure of approximately the upstream pressure P_1. The distance from the nozzle to the Mach disk can be calculated in the case

of a free jet expansion (in absence of the substrate) and is equal to 12 mm for a 250 μm orifice. The nozzle-to-substrate distance has been set at 1.2 mm.

The maximum gas velocity can be determined and is equal to:

$$v_{max} = \sqrt{\frac{2\gamma k T_0}{(\gamma - 1) M_a}} \quad (4.1)$$

where γ is the ratio of heat capacities of the gas, k is Boltzmann's constant, T_0 is the stagnation gas temperature, and M_a is the molecular mass of the gas.

The NPs do not reach the maximum gas velocity because as the gas is accelerated, the density and temperature drops, and thus the drag force that accelerates the NPs drops as well. The maximum velocity and kinetic energy of the NPs can be calculated. For helium carrier gas accelerated through a flat plate nozzle with an upstream-to-downstream pressure ratio of ~5000 (as is used in this work), the maximum energy reached by the NPs is in the range of 0.5-1 eV/atom. In addition, it has been shown that virtually none of this kinetic energy is dissipated at the NPs cross the bow shock where the gas recompresses above the substrate surface. Thus, the particles strike the substrate with very close to their maximum speed.

4.1.2 Impaction of NPs on a substrate

Various studies that utilized MD simulations [5]-[8] predict the behavior of impacting NPs. An interesting review has been published by Nordlund [5], who compiled results obtained for a wide range of NPs sizes and impaction energies (see Figure 4.1).

Figure 4.1: Impaction regimes of nanoparticles (reprinted from [5])

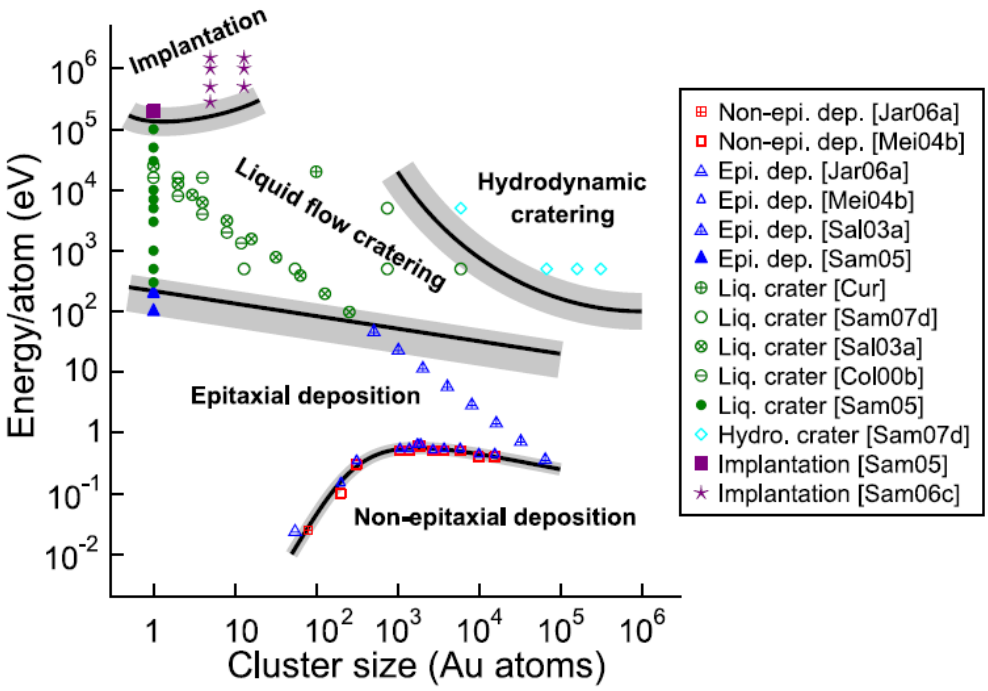

Five impaction regimes can be distinguished. In the low energy regime, non-epitaxial deposition (or soft landing) occurs where the crystalline structures are not affected by the impaction process but the particles stick to the substrate. At higher energies, MD simulations predict epitaxial deposition, when the kinetic energy is sufficient to allow the reorganization of the crystal lattice of the NP upon impaction and to align with the crystal lattice of the impacting substrate. In this work, the predicted impaction regime is at the limit ofnon-epitaxial or epitaxial deposition since the NPs contain roughly 10^5 atoms and impaction energy is in the range of 0.5-1 eV/atom (assuming we can extrapolate the results presented by Nordlund to Ag). Other impaction regimes occur at much higher impaction energies and are not relevant for this work.

4.2 Influence of experimental parameters on the deposition efficiency of NPs and comparison with MD simulations from the literature

4.2.1 Influence of the nozzle-to-substrate distance

A series of lines have been deposited on substrates where the nozzle-to-substrate distance was varied. The variation in nozzle-to-substrate distance was achieved by stacking of substrates to form steps. By translating the stage under the NP jet across the steps, the resulting lines were deposited with different nozzle-to-substrate distances. Thus, all other parameters could be kept constant. The Ag lines were deposited onto Si substrates and Si substrates that were coated with Au/Pd by Ar-sputtering of the substrates. The thickness of the Au/Pd coating has not been measured, but the deposition parameters are given in section 2.5.

Figure 4.3a shows the film width (measured from width at the base of the line) as a function of nozzle-to-substrate distance. The plot shows that the film width is proportional to the nozzle-to-substrate distance, and that the lines are always wider when deposited on Au/Pd-coated Si substrates compared to bare Si substrates. The proportionality between the film width and the nozzle distance suggests that the critical impaction angle for NPs to stick (defined on Figure 4.2) is constant for a given substrate (Figure 4.3b). It is also apparent from Fig. 4.3b that the critical angle is larger for Au/Pd-coated substrates than for bare Si substrates.

Figure 4.2: Definition of the NP jet angle and critical angle for sticking of NPs

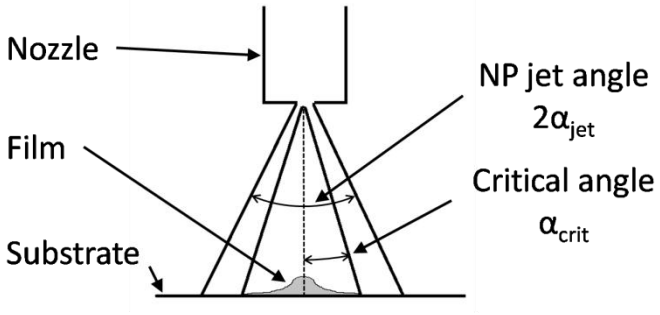

Figure 4.3a Influence of the nozzle-to-substrate distance on the width of the films. The legend refers to gold-coated silicon and bare silicon substrates.

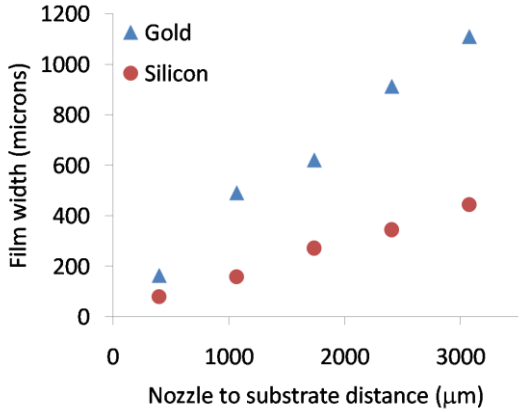

Figure 4.3b influence of the nozzle-to-substrate distance on the critical angle for sticking of NPs. The legend refers to gold-coated silicon and bare silicon substrates.

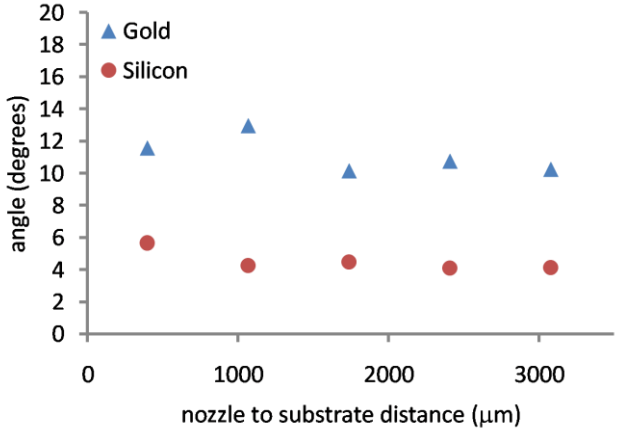

In the model proposed by Huang (see section 4.1.1), 5 nm NPs impact at a velocity of ~1000 m/s, independently of the nozzle-to-substrate distance (within the range of nozzle distances used here), and the normal of the NP velocity vector is considered to be independent from the impaction angle (since the impaction angle is very small). The data shown in Figure 4.3b validate these hypotheses since the critical impaction angle to get sticking of the NPs seems to depend only on the substrate material. The critical impaction angle obtained for Au/Pd substrates is bigger, which suggests that NPs stick more easily on this surface than on bare Si. During the impaction process, initial rearrangement of the atoms in contact with the substrate is critical for obtaining sticking of the particle [7] (see also Figure 1.5). The Ag atoms of the NPs are thus more likely to bond to the Au or Pd atoms of the coated samples than to the Si/SiO_2 at the surface of the bare Si sample.

We can also conclude that NPs impaction is governed by the normal velocity. According to the data presented here, and considering a 5 nm particle impacting at V=1000 m/s, the normal velocity at the critical angle is $V \cdot \cos(\alpha_{crit})$=1000 m/s for bare Si and 980 m/s for Au/Pd-coated Si.

4.2.2 Influence of impaction substrates

A series of lines have been produced on a silicon substrate partially coated with a thin layer of Au/Pd to study more carefully the influence of this metallization on the sticking of the NPs. An observation with an optical microscope and a SEM revealed that the films were significantly wider on the area coated with Au/Pd, as showed on Figure

4.4. This shows directly that (1) the NPs adhere better on the Au/Pd coating than on the bare Si/SiO_2, and (2) a fraction of the NPs cannot adhere on bare Si/SiO_2 when the impaction angle is greater than a certain value.

Figure 4.4: Film written on Bare Si and Au/Pd coated Si (Plan view)

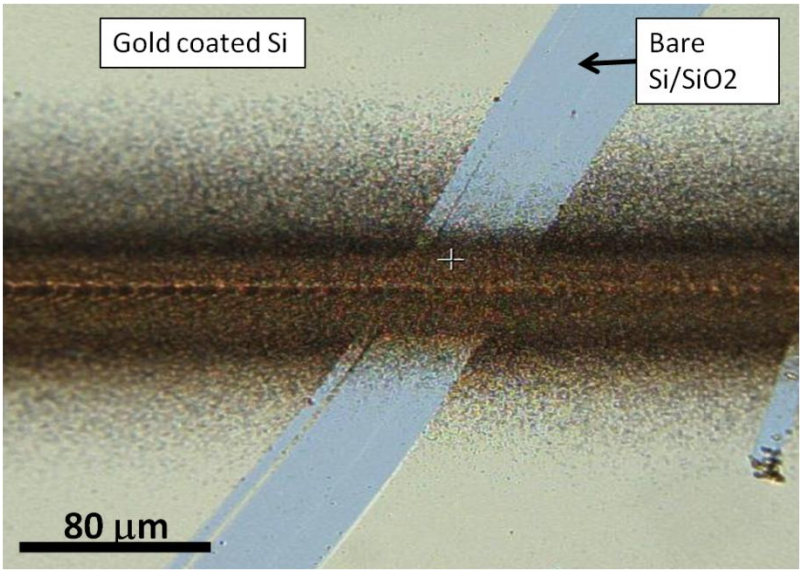

The formation of the films occurs in two successive steps: First, the formation of the first layer of NPs on the substrate, where impacting NPs can either bounce off, land in a non-epitaxial configuration, or land in an epitaxial configuration. Then, the lines build up on top of the already existing silver layer. It is assumed that the nature of the substrate can affect the first step of the film formation, but has little influence on the second step. Also, we can hypothesize that the deposition on the Au/Pd layer mimics the deposition on existing layers of Ag NPs since in both cases, the silver is impacting onto a metal surface. The probability of sticking for the 1st layer is thus lower than for subsequent layers when

depositing onto a bare silicon surface. From MD simulations data, it can be expected than the probability of sticking onto subsequent layers or onto a metalized surface is higher since it more likely to form bonds with the substrate.

We can estimate the ratio of the sticking probabilities onto Si and onto an Au/Pd layer (p_1 and p_2, respectively) by estimating the mass deposited per unit length in the following geometry:

Figure 4.5: Definition of angles and distances for a silver line

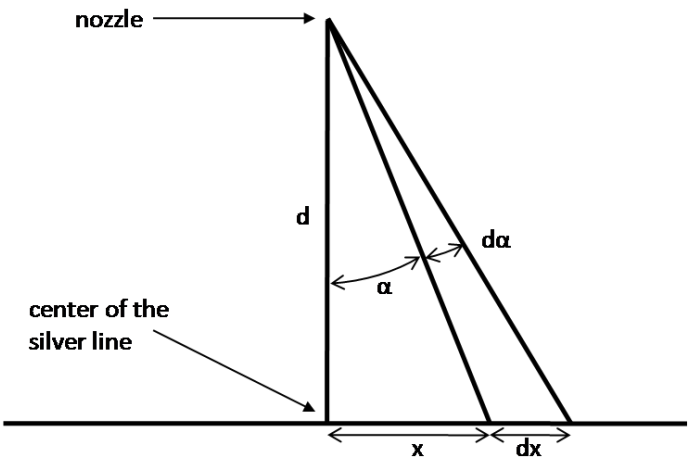

At any instant, the mass of nanoparticles in the aerosol between the angles α and α+dα is equal to:

(4.2) $$d\alpha \cdot D_a(\alpha)$$

Where $D_a(\alpha)$ is the aerosol density at the angle α. The mass deposited on the line between a distance x and x+dx is proportional to the mass given by (4.2) and the probability of sticking for a given substrate (p):

(4.3) $$d\alpha \cdot D_a(\alpha) \cdot p$$

We can then calculate the mass deposited per unit length at a distance x from the center of the line:

(4.4) $$\frac{d\alpha . D_a(\alpha) . p}{dx}$$

which simplifies to:

(4.5) $$\frac{D_a(\alpha) . p}{d \cdot \cos(\alpha)}$$

At the edge of the line, the line density for which the line is not visible anymore is equal for lines deposited onto either Si or Au/Pd substrates, then:

(4.6) $$\frac{D_a(\alpha_1) . p_1}{d . \cos(\alpha_1)} = \frac{D_a(\alpha_2) . p_2}{d . \cos(\alpha_2)}$$

where α_1 and α_2 are the impaction angles at the edge of the silver line and are given in Figure 4.3b. If we assume that the aerosol density is the same at both angles, we get a ratio of sticking probabilities for both substrates approximately equal to:

(4.7) $$\frac{p_1}{p_2} \simeq \frac{\cos(\alpha_1)}{\cos(\alpha_2)}$$

which is equal to 0.98. Thus, even if the lines are significantly wider when deposited on Au/Pd than bare Si, the sticking probability is not very different.

4.2.3 Influence of the substrate temperature

Lines have been written at two different temperatures (25°C and 75°C) on bare Si/SiO_2 substrates. Other parameters were kept constant (feed rate of 10 mg/hr, 20 passes

and substrate translation speed of 0.635 mm/s). It was hypothesized that increasing the substrate temperature would increase the sticking of the NPs, since more of the heat coming from the impaction goes into heating the particle and less goes to heating the substrate. NPs are thus more likely to melt or form a chemical bond. The hot particles/substrate is also more compliant (lower Young's modulus) at higher temperatures.

Figure 4.6: Cross section of lines written at two different temperatures

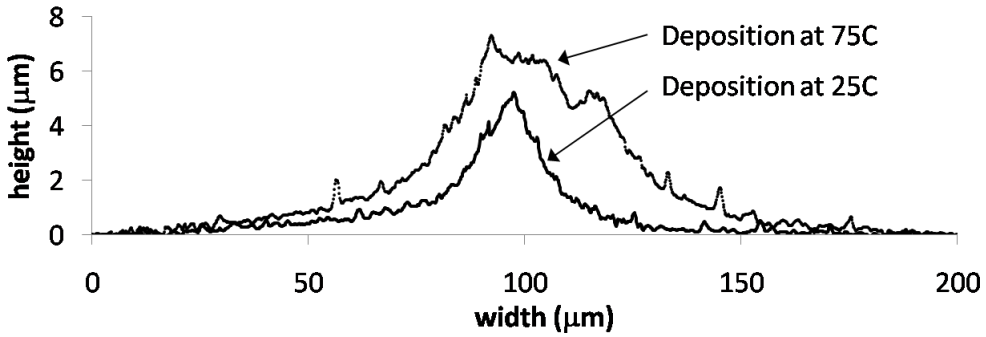

Writing thick films enabled the measurement of the cross sections of the films using a profilometer and therefore allowed the comparison of the sticking efficiency as the substrate temperature was varied. Figure 4.6 shows that a film deposited on a substrate heated at 75°C resulted in a film with a cross section that was about 1.5 larger than a film deposited at room temperature.

We can conclude that a large fraction of NPs adhere upon impaction when the substrate is heated. This is consistent with predictions made by Nordlund [5], who suggested that the minimum energy per atom required for epitaxial deposition of a NP impacting with a kinetic energy E_k:

(4.8) $$\frac{E_k}{N} = \frac{1}{c}\left[3k(T_{melt} - T_i) - \frac{\Delta E}{N}\right]$$

where N is the number of atoms per NP, T_i and T_{melt} the initial and melting temperatures of the NP, ΔE the surface energy change, and c the fraction of kinetic energy converted to heat in the particle, the rest of the kinetic energy goes to heating the substrate and to shock waves created upon impact. This model is consistent with the experimental results presented above, since increasing the substrate temperature most likely increases the value of c, and thus decreases the energy required for epitaxial deposition.

4.2.4 Film density

A thick square-patterned film had been deposited to measure its density. Instead of simply translating back and forth the substrate under the NP jet, the X-Y stage has been programmed to write a square spiral with a pitch of 10 µm. Each line of the spiral has been written with 29 passes. This way, enough material has been deposited so that the film could be weighted. The volume of this film has been measured using an optical profilometer. Using this method, the as-deposited relative density is calculated to 68% (±4%). This compares with a value measured by Albert [9] of 70% relative density for similar silver films produced by LAMA using an indirect method relying on conductivity.

The formation of porous films at these impaction energies is also in qualitative agreement with MD simulation data, even if there is a difference in predicted final density. Indeed, no data for silver were available, which made any comparison difficult.

For instance, Haberland [6] predicted the formation of Mo films that are ~80% of bulk for the energy range of 0.5-1 eV/atom and smaller particles (10^3 to 10^4 atoms, or 2-3 nm in diameter).

4.3 Conclusions

Several conclusions can be drawn from these experiments. First, it has been shown that the nature of the substrate has a significant influence and therefore must be well chosen to maximize the collection efficiency of particles. This is because the initial rearrangement of atoms in the NP upon impact is critical to get sticking [7]. Increasing the substrate temperature also increases the probability of sticking, not only during the initial layer deposition but also during the subsequent build-up of the film. It is therefore an effective and practical processing parameter to vary if thick films are to be deposited.

5. Deformation of nanostructured silver

This chapter focuses on the deformation of porous nanostructured silver in compression. First, the results of the compression experiments are presented. Then, densification of this material under various compression conditions is analyzed in attempt to determine the dominant densification mechanism. Finally, the possibility of using the LAMA process to produce lines that can be compressed to create a seal is demonstrated. Such a process would be useful for a MEMS sealing application.

5.1 Compression experiments

A series of silver lines have been produced using LAMA with the following processing conditions: a feed rate of 15 mg/hr, 30 passes, a writing speed of 6.35 mm/s, and a nozzle-to-substrate distance of 1.2 mm. Under these processing conditions, the lines were produced from a mixture of individual NPs and agglomerates. Micrographs of the lines show clearly the presence of the large agglomerates. Compression experiments at various loads, compression times, and temperatures are presented in the following three sections.

5.1.1 Compression of lines at room temperature with increasing loads

Silver lines were compressed at a rate of 0.1 mm/min until the final load was reached, and the final load was held for 10 s. Under such short deformation times, time-dependent deformation mechanisms (like creep) are not expected to play a significant role so deformation is expected to be dominated by yielding (plastic deformation).

The experiments presented in Figures 5.1 and 5.2 clearly show that the top of the line is deformed during the compression experiments and results in a "flat top" that matches the surface of the punch used to perform the compression experiments. The magnitude of the deformation increases with compression load (the applied load was 5N for the sample in Figure 5.1, and 65N for the sample in Figure 5.2).

Figure 5.1: Optical micrographs of a silver line after compression at 5 N a) plan view b) oblique view c) cross-sectional profile

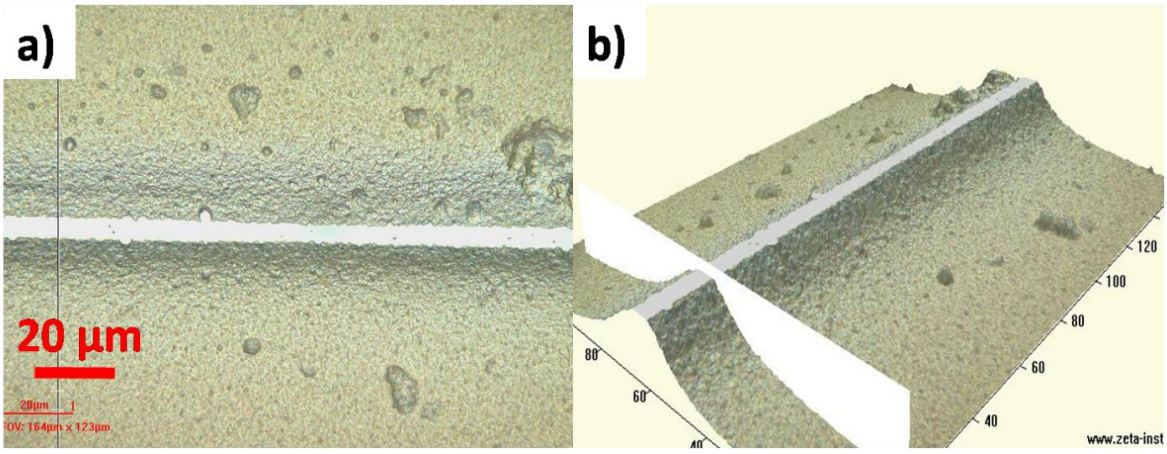

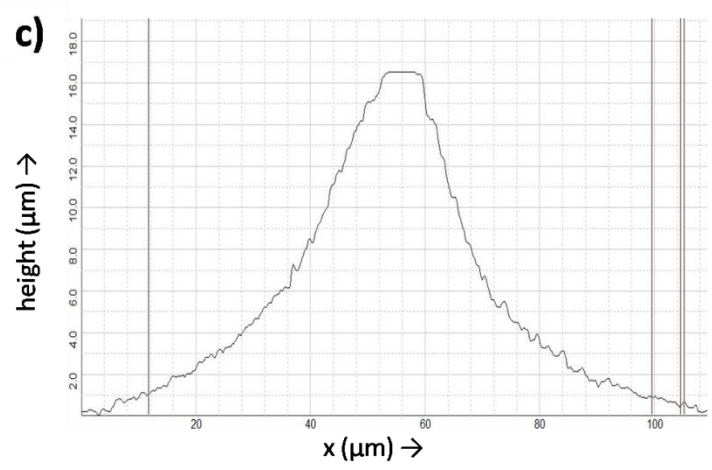

Figure 5.2: Views of a silver line after compression at 65 N

plan view b) oblique view c) cross-sectional profile

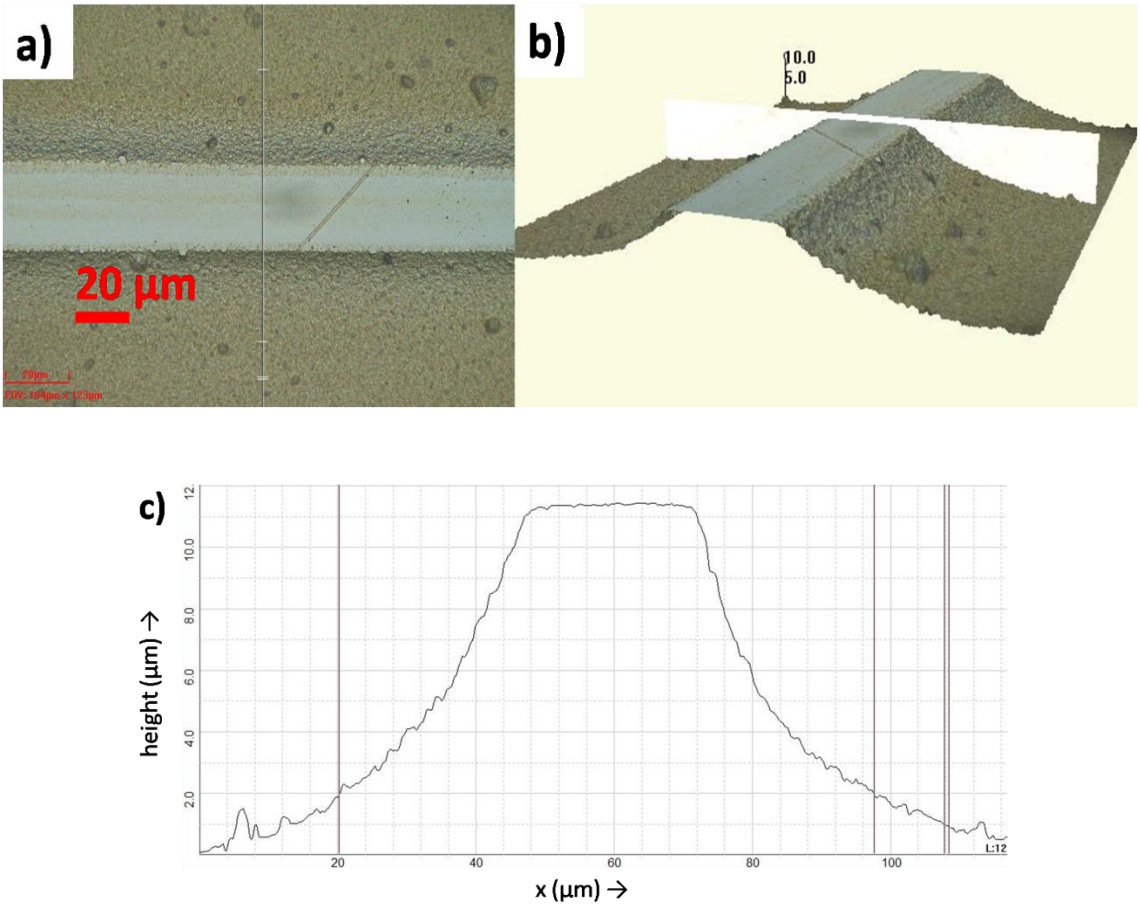

In Figure 5.3, the evolution of the cross-section of a line is shown for increasing loads. The profilometer scan was conducted at approximately the same location after each compressive step (± 1 µm) enabling the measurement of the cross-sectional area. The changes in cross-sectional area are shown in the second row of Table 5.1. These numbers are used to calculate the changes in average density of the line, which are given in the last row of Table 5.1. The densification numbers are calculated by assuming that

the initial average density is 70% of fully dense silver, and considering that the reduction in cross-sectional area is caused by densification. This will be discussed later in Section 5.2, which focuses on the densification of the lines.

Figure 5.3: Evolution of the line cross section with increasing loads

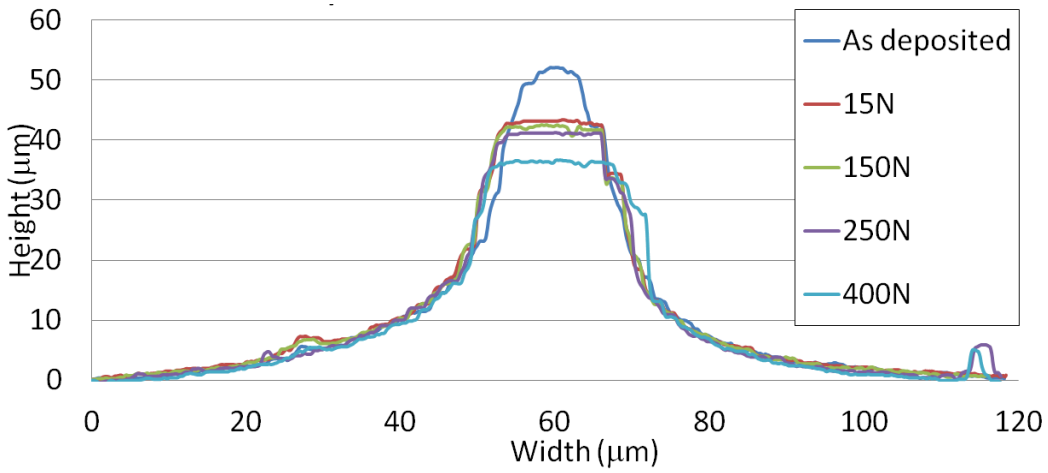

Table 5.1: Cross section evolution of a silver line compressed at room temperature with increasing loads

Load (N)	0	15	150	250	400
Cross section area (μm^2)	1323	1325	1299	1262	1189
Average relative density (% of bulk density)	70	70	71	73	78

A similar study has been conducted to study the morphology evolution of silver lines under very high loads and the change in morphology is presented schematically in Figures 5.4.1 -5.4.3. Under extreme loads, the lines undergo a very high strain. Starting at 300N (corresponding to Figure 5.4.3), the outside regions at the base of the line starts delaminating from the substrate, but the line itself remains self-standing and the center of

the line still adheres to the substrate (as can be seen on Figure 5.5). In the cross-sectional profile of the lines shown in Figure 5.6, these “wings” are apparent on the sides of the line corresponding to regions where delamination has occurred. Since the profilometer only acquires projected views from above the line, the regions of the line that have lifted off the surface beneath the “wings” are not apparent in the cross-sectional views from the profilometer.

The final stress corresponding to each load has been calculated by measuring the compressed zone area with an optical microscope after deformation and dividing the load by this area. The data are shown in Table 5.2. Table 5.2 gives also the average density changes after compression at 100N and 300N. No densification data are given for 500N and 700N, since the partial delamination of the line made prevented any measurement of the cross-sectional.

Figure 5.4: Partial delaminating of a silver line upon compression under large loads

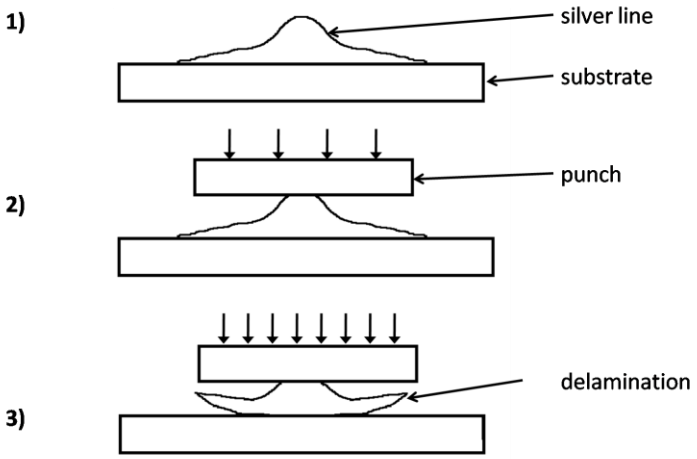

Figure 5.5: Bottom view of a fully delaminated silver line (obtained with an optical microscope) a) The grey region on the left is the Si substrate b) Close up of the same sample shown in a). The region in the center remained in contact with the substrate upon compression, as the zones on the sides delaminated from the substrate.

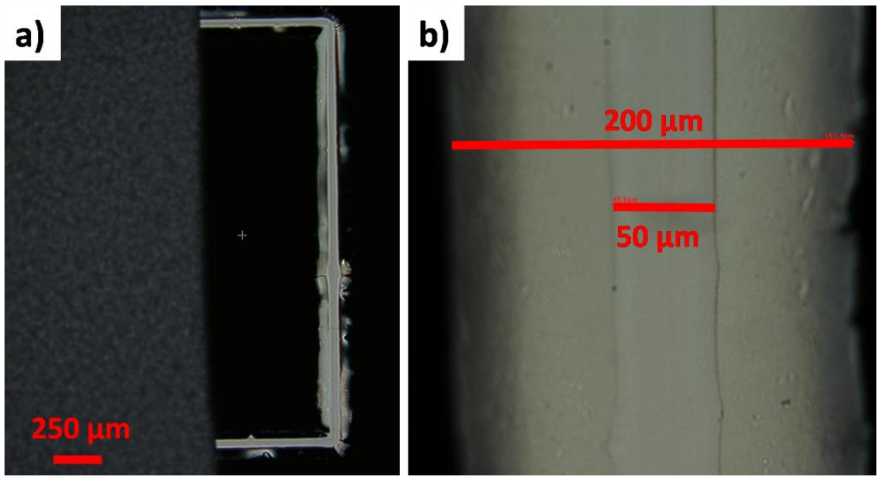

Figure 5.6: Profile evolution of a line compressed at room temperature

Under high loads

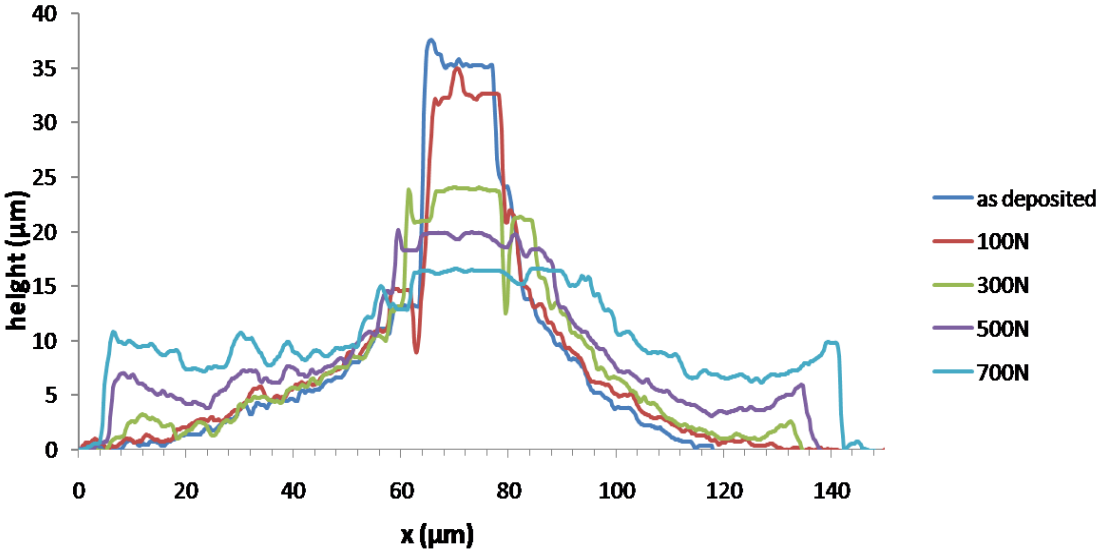

By comparing the cross-sectional profiles after compression at 500 N and 700 N, it is apparent that the width at the base of the line increases (the lines expands outwards from the center of the line). Thus, the final morphology is a combination of two different mechanisms: (1) the delamination of the "wings" and (2) flow of matter from the central region of the line to the sides of the line.

Table 5.2: Final stresses applied to a silver line compressed at room temperature under high loads

Load (N)	0	100	300	500	700
Approximate stress (MPa)	-	700-1080	2050-3250	$\geq$ 3400	-
Relative density (% bulk)	70	70	73	-	-

5.1.2 Compression of lines at room temperature for different loading times

To see if time-dependent deformation mechanisms are occurring at room temperature during compression of nanostructured silver, a silver line was compressed at a rate of 0.1 mm/s and the load was then held for 15 min. A surface profile of the line was then acquired with the optical profilometer and the sample was loaded again at the same load for an additional hour. Any additional strain observed after the first experiment is due to time-dependent deformation. The results, shown in Figs. 5.7 and 5.8 show little difference in the height or profile of the line. We can estimate the creep rate at room temperature by doing the following calculation:

(5.1)
$$\dot{\varepsilon}_{max} = \frac{\varepsilon}{t} = \frac{\Delta h/h}{t} = \frac{3\ \mu m/20\ \mu m}{2700\ sec} = 6 \times 10^{-5}\ s^{-1}$$

Figure 5.7: Profile of a silver line compressed at room temperature for 15 min with a load of 100N. Blue: before compression; red: after compression

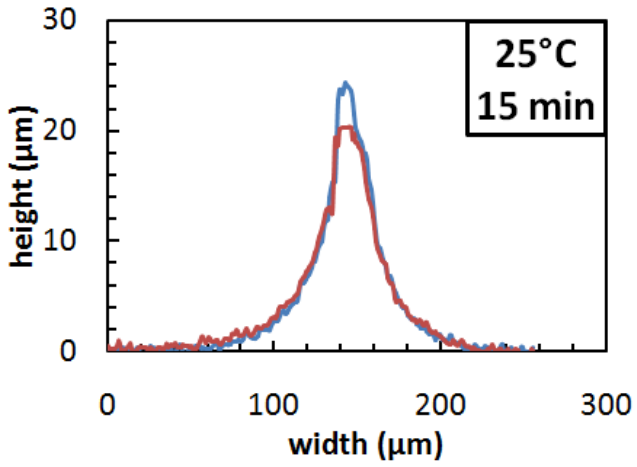

Figure 5.8: Profile of the same silver line as shown in Figure 5.7, loaded at 100N for another 45 min. Blue: before compression; red: after compression

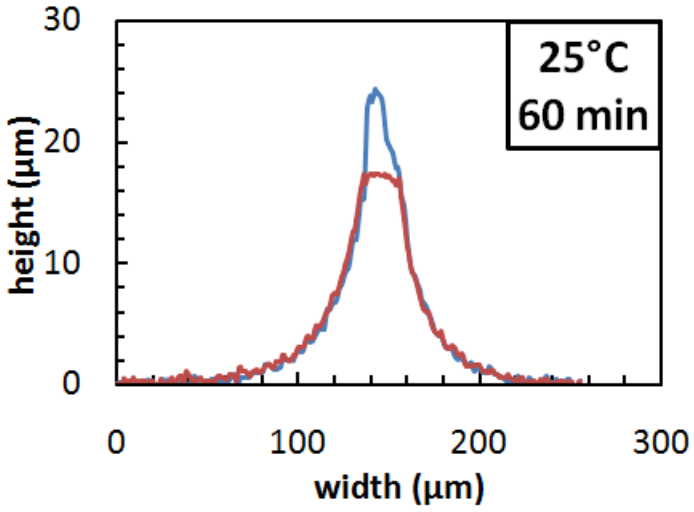

5.1.3 Compression of lines at 150°C with different loading times

To study the influence of temperature on the deformation of silver lines, compression experiments were carried out at 150°C.This temperature was selected because a previous study [10] has shown that significant pressureless sintering begins at this temperature, but grain growth is still very limited. The samples were compressed at a rate of 0.1 mm/min until a load of 100N was reached. The load was either held for 15min or 60min, to determine the relative contributions from plasticity and from time-dependent deformation at this temperature. Figures 5.9 and 5.10 show a line compressed during 15 min and Figure 5.11 and 5.12 show a line compressed for 1hr.

Figure 5.9: Micrograph obtained from profilometer of a line a) before and b) after compression at 100 N (1320-1350 MPa) and 150°C for 15 min

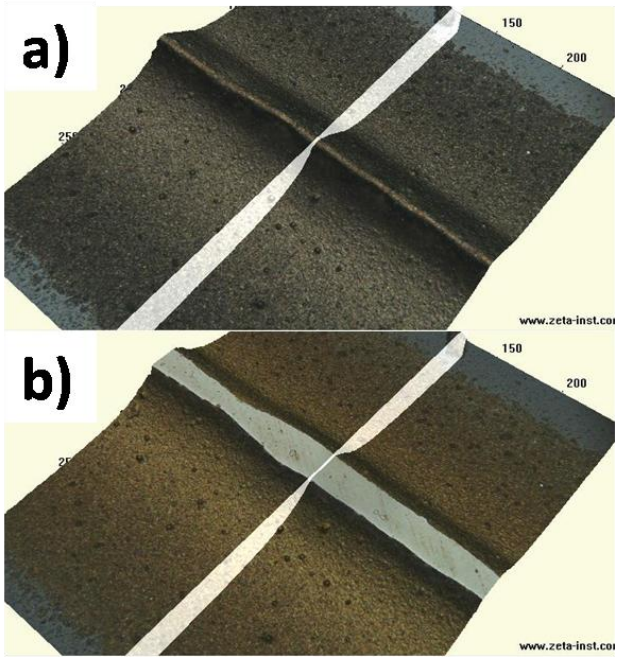

Figure 5.10: Evolution a silver line profile after compression at a stress of 1320-1350 MPa and temperature of 150°C for 15 min

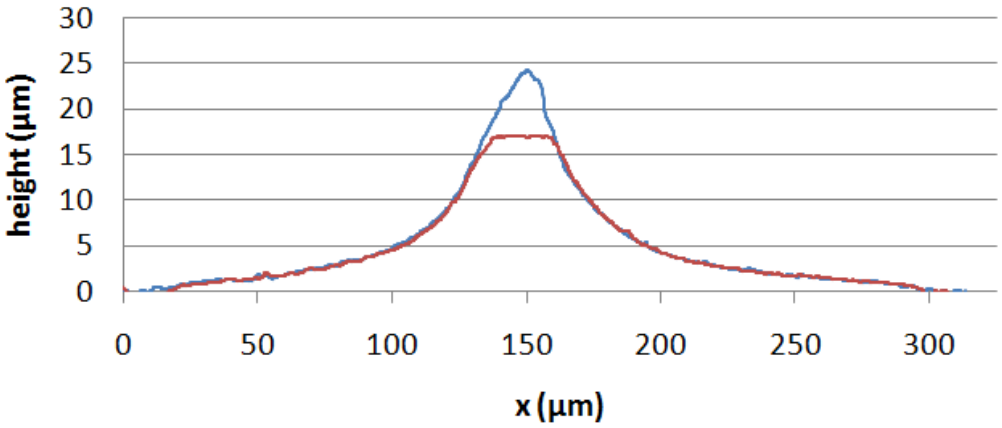

Figure 5.11:Micrographs of a line a) before andb) after compression at 150°C for 60 min, under 100N (610-654 MPa)

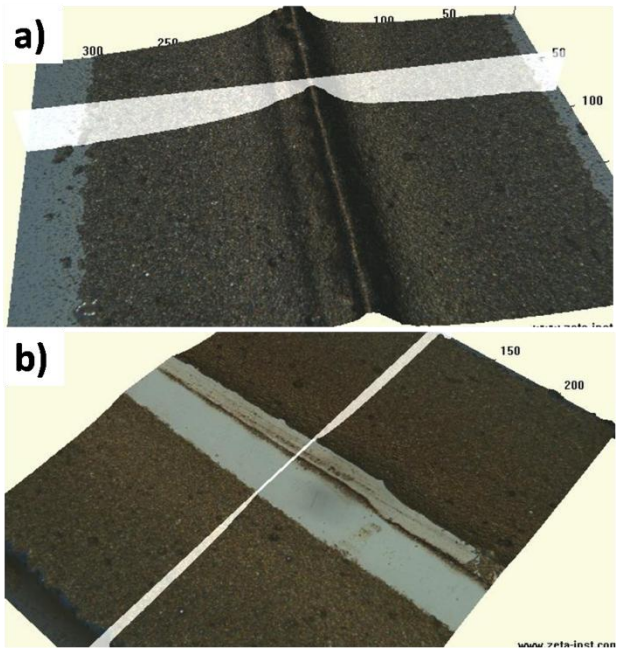

Note: This sample, rather than exhibiting a typical pseudo-Gaussian cross-sectional profile exhibited a double peak, which is visible both on 5.9a and 5.9b.

Figure 5.12: Evolution of a silver line profile after compression at 150°C for 60 min, at 100N (610-654 MPa). The profile with the flat top corresponds to the profile after compression

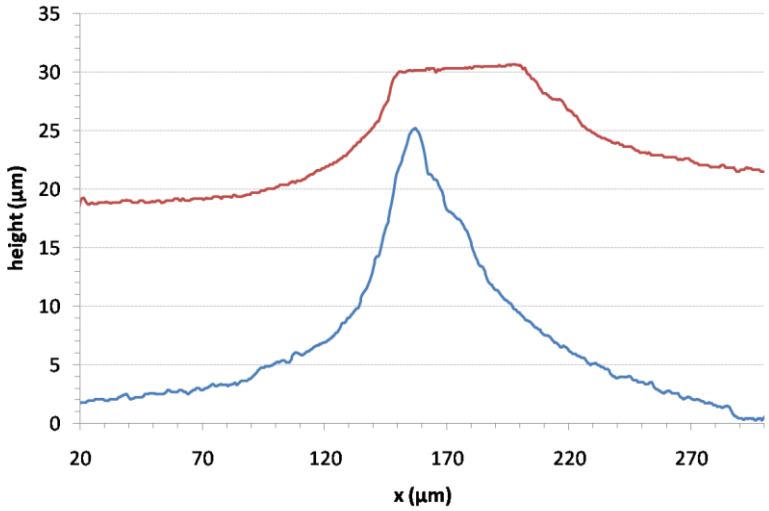

The sample shown in Figure 5.12 delaminated from the substrate completely after compression. This is why the profile of the compressed line appears above the profile of the uncompressed line (the origin in height is the silicon substrate for both profile lines). The change in the cross-sectional area could not be measured since the profilometer only acquires plan views from the line of the line and does not "see" the empty region beneath the line. Nevertheless, it is clear that the final strain is much larger after compression for 60 min than for 15 min (Figure 5.10). A direct measure of the additional strain that occurs with time is the difference in the heights of the lines. The initial height of the line was about 25 µm and the final height of the line was ~17 µm after 15 minutes and was ~10 µm after 60 minutes This difference in strain as the loading time increases, but the applied load stays the same, confirms that a time-dependent mechanism is contributing to the observed total deformation.

The strain rate at 150℃ can thus be estimated by dividing the strain occurring between a 15 min compression and a 60 min compression by the time deformation, 45 min:

$$\dot{\varepsilon}_{max} = \frac{\varepsilon}{t} = \frac{\Delta h/_h}{t} = \frac{(17-10)\ \mu\text{m}/_{25\ \mu\text{m}}}{(60-15)\times 60\ \text{sec}} = 1.0\times 10^{-4}\text{sec}^{-1} \quad (5.1)$$

Further discussion about the deformation mechanisms that cause the time-dependent deformation are provided in Chapter 6.

5.2 Densification of porous nanostructured silver

5.2.1 Average density

The relative change in average density is determined from the measured initial and post-compression cross-sectional areas to quantify the change in volume. The change in relative density is then calculated by assuming that the initial relative density is 70%. This initial density is in agreement with separate density measurements (see section 4.2.4, or reference [10]). The following equation gives the average density after compression (D_f):

$$D_f = D_0 \times \frac{A_f}{A_0} \tag{5.2}$$

where D_0 = 70%, A_0 and A_f are the initial and final line cross sectional areas, respectively. Both are measured by integration of the profile scans obtained with the profilometer.

Tables 5.1and 5.2 give the evolutions of the average relative densities of lines compressed at room temperature under increasing loads. The relative densities for lines compressed at 150°C are presented in Table 5.3. It is apparent from the data that enhanced densification occurs at 150°C, since a final average density of 75% was observed after compression at ~1230 MPa, whereas a final average relative density of only 73% was measured after compression at ~2650 MPa at room temperature. Two potential reasons for the enhanced densification are 1) a significant decrease in yield stress at 150°C relative to room temperature, 2) or the activation of a time-dependent

deformation mechanism at 150˚C that provides and additional mechanism for deformation beyond plasticity. The possibilities will be explored in more detain in Chapter 6.

5.2.2 Local variations in densification

In the previous section, we have characterized the lines based on their average density. In reality, the density is likely to vary with position within the line. When the lines are compressed since the stress distribution is not uniform (it is rather parabolic), resulting in non-uniform densification. The average density method is too coarse and needs to be refined to better understand the densification process.

Since the densification is likely non-uniform, the change in relative densities presented in Table 5.1-5.2 represents a lower bound to the maximum amount of densification in the line. The densification is most likely much higher locally, at the center of the line, where the stress is the highest and lower away from the center.

From Figure 5.13 it is clear that no deformation occurs outside of the region located beneath the upper punch. Therefore we can assume that densification occurs only in the region under the punch (For Fig. 5.13, the region located between x = 120 μm and x = 160 μm). We can also assume that densification is uniaxial, occurs in the same direction as the applied load, and is proportional to the shrinkage in height. Under these assumptions, the final density at the position x is given by:

(5.3) $$D_f(x) = D_0 \times \frac{h_f(x)}{h_0(x)}$$

where D_0 = 70%, and $h_0(x)$ and $h_f(x)$are respectively the initial and final line height at the coordinate x. Figure 5.13 shows the densification region, and Figure 5.14 the variation in density along the cross section of the same sample compressed at 150°C

Figure 5.13: Regions in a compressed silver line where densification is assumed to occur

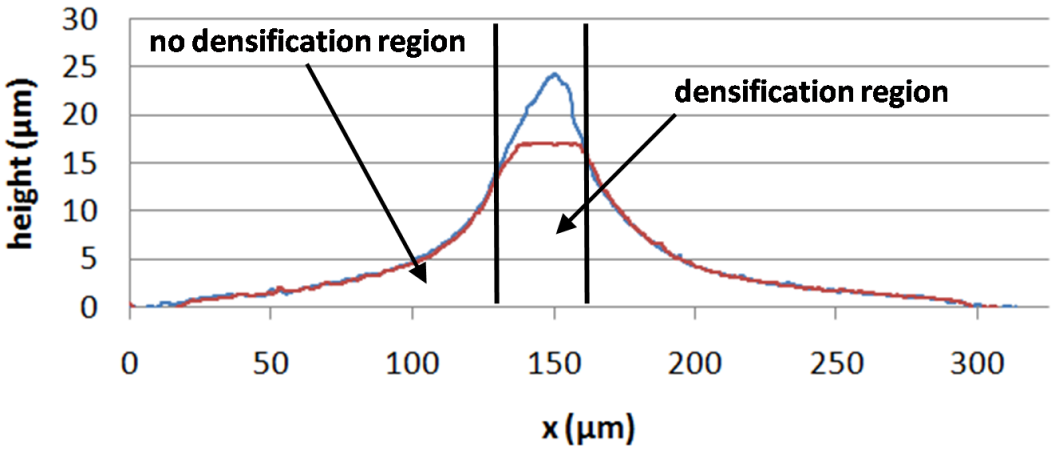

Figure 5.14: Variation in final density along the cross section of a compressed silver line using the approximation given in Equation (5.2) (same sample as shown in Figures 5.8 and 5.13)

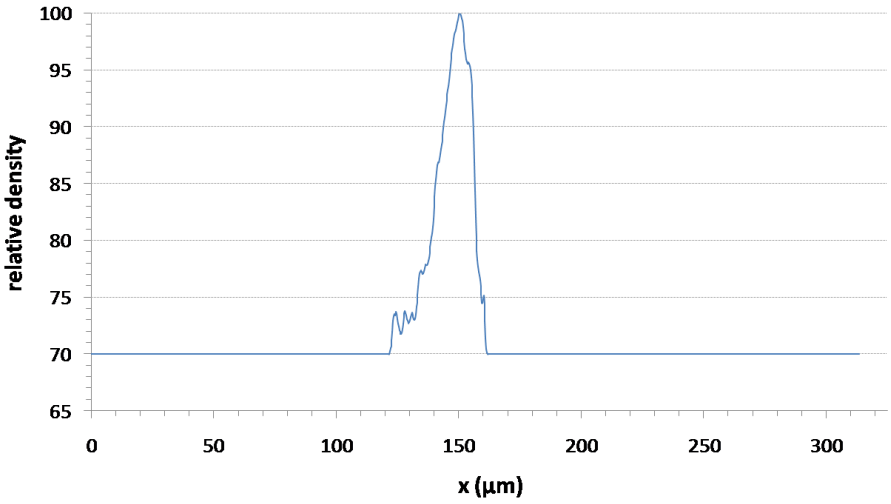

Figure 5.14 clearly shows that the samples undergo very high densification locally. Full density is even reached right below the indenting punch.

Tables 5.3 and 5.4 summarize the densification data obtained from compression experiments conducted at 150°C and room temperature. The experiments conducted at 150°C were conducted varying the time, and experiments conducted at room temperature show the influence of increasing applied load. Densification seems to be increased when raising the temperature: indeed, obtaining a comparable final density requires to apply a much higher stress at room temperature than at 150°C.

Table 5.3: Densification of silver lines after compression at 150°C during various times (experiment shown on Figure 5.10)

Time	Before compression	15 min	60 min
Applied stress	-	1320-1350 MPa	610-654 MPa
Average relative density	70%	75%	Not measurable
relative average density in the region below the indenting punch	70%	83% (100%, locally)	Not measurable

Table 5.4:Densification of silver lines after compression at room temperature at various loads (experiment shown on Figure 5.6)

Time	Before compression	100 N	300 N
Applied stress	-	700-1080 MPa	2050-3250 MPa
Average relative density	70%	70%	73%
relative density in the region below the indenting punch	70%	70%	~86%

5.2.3 Conclusions

Compression experiments were carried out on porous nanostructured silver lines varying the process temperature and the loading time. Local densification of the lines was observed and quantified. Both varying parameters were proven to have a significant influence on the deformation. An improved densification during compression has been observed when the process temperature was raised from room temperature to 150°C (see Tables 5.3 and 5.4). The loading time also has a big influence on the process: at 150°C, samples held under 100N loads for 60 min exhibited a much larger final strain due to the compression than samples held for only 15 min, which proves that time dependent deformation is critical at this temperature. The strain rate associated with this time-dependant mechanism has been estimated to 10^{-4} s^{-1}.

Beyond the experimental results, this study shows that one can take advantage of the geometry and porosity of the silver lines: if the process conditions are well chosen, the lines can be deformed and densified at relatively low temperatures and low compressive loads to get a flat top that matches perfectly the indenting surface. An example of an application using these unique features is presented in the next section.

5.3 Square pattern compression for MEMS sealing applications

In addition to individual lines, squares have been written, with the intention of demonstrating that the direct writing process can provide viable sealing solutions for MEMS devices. For instance, hermetic sealing may be possible by writing uniform lines of nanostructured silver around a MEMS or integrated circuit (see Figure 5.14). Then, low temperature wafer bonding on top of the lines allows the MEMS device to be sealed.

Figure 5.15: MEMS Packaging using silver lines

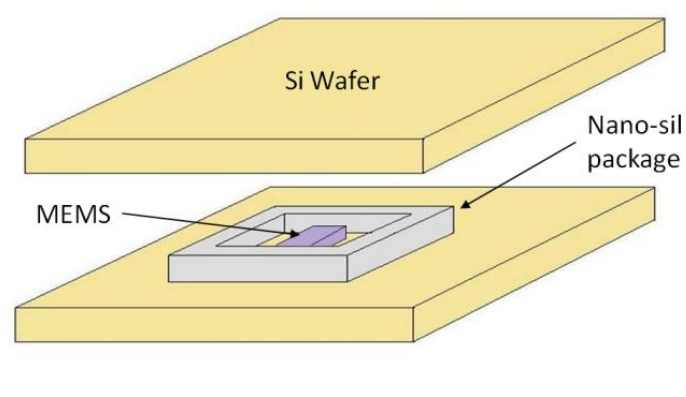

Figure 5.16 shows a top view of a square of silver lines. After compression by a punch, the lines were 18 µm high (± 3.5 µm). This spatial precision is good enough to envision hermetic sealing. This process creates a contact region between the silver line and the top wafer that is continuous (no gaps), which is presumably good for sealing. In these experiments, sticking/bonding to the top substrate was prevented by the use of a glass slide, to look at the line deformation. To get bonding, a metallic material would be more appropriate.

Figure 5.16: Square of silver lines after compression at 700N

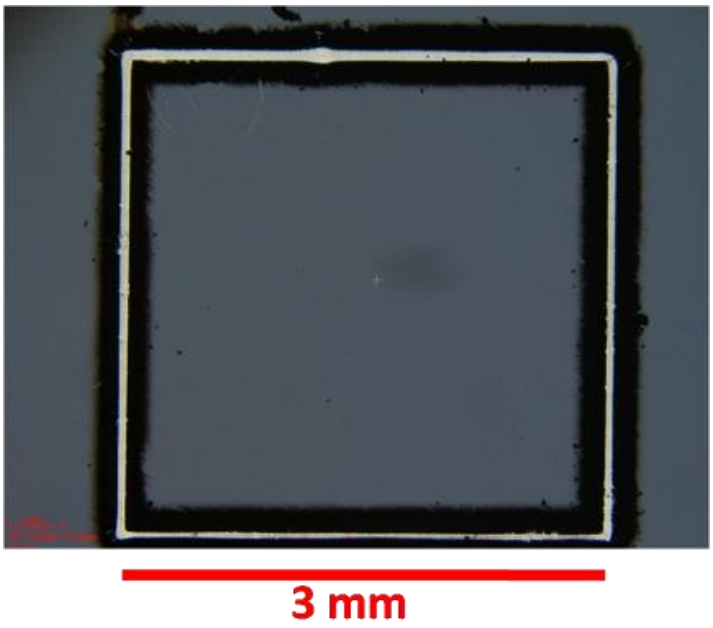

6. Modeling of the densification process

To understand the mechanisms involved in the deformation of porous nanostructured silver and the observed densification under compressive stress, a model developed by Ashby [12] to predict pressure-assisted sintering of microcrystalline powder compacts has been adapted to nanocrystalline silver. Section 6.1 briefly describes the geometry of this model, while Section 6.2 discusses the possible mechanisms leading to densification. Section 6.3 presents a map that predicts the dominant densification mechanisms for lines as a function of density of the lines and the applied pressure and compares these predictions with the experimental data presented in Chapter 5.

6.1 Geometry of the model

This section highlights the basic concepts and main equations of a model developed by Ashby. Details and derivations of the equations can be found in [12].

The starting material is a compact made of randomly packed, uniformly sized particles, with an initial density D_0=0.64. The initial particle size, R, is considered to be 5 nm.

The densification is first modeled empirically so that it is independent of the actual densifying mechanism, by relating the densification rate, $\dot{D}$, and the linear shrinkage rate of the compact, $\dot{y}$.

For relative densities below 0.9 (first stage), the densification of the compact is modeled by allowing the particles to grow in size around fixed centers. The densification rate, $\dot{D}$ and linear shrinkage rate of the body $\dot{y}$ are related by:

(6.1) $$\dot{D} = 3 \cdot (D^2 \cdot D_0)^{1/3} \cdot \frac{\dot{y}}{R}$$

where R is the initial particle radius. Also, the number of contacts between the spheres (Z) grows and can be calculated. If this is allowed to proceed, the neighboring spheres will overlap, which is non-physical. To prevent this from occurring, this volume has to be removed and the derivative of this volume gives the excess volume per second that has to be removed by any densifying mechanism.

It can also be shown that an external pressure, p, applied on the random powder network produces an average contact force given by:

(6.2) $$f = \frac{4 \cdot \pi \cdot R^2}{Z \cdot D} p$$

where Z is the number of contacts between spheres and is given by:

(6.3) $$Z = Z_0 + C\left(\left(\frac{D}{D_0}\right)^{1/3} - 1\right)$$

where Z_0=7.3 and C=15.5.

The effect of surface tension as an additional driving force is also taken into account, leading to an effective pressure at the particle contacts given by:

(6.4) $$p_1^{eff} = \frac{4 \cdot \pi \cdot R^2 \cdot p}{a \cdot Z \cdot D} + p_s$$

where a is the area of a contact between two particles and p_s is given by:

$$p_s = \gamma_s \left(\frac{1}{\rho} - \frac{1}{x}\right), \qquad \rho = \frac{x^2}{2(R-x)} \tag{6.5}$$

In the final stage of densification (D>0.9), the compact is modeled as a homogeneous solid containing spherical voids that are located at the corners of tetrakaidecahedral particles. In this geometry, the effective pressure is given by:

$$p_2^{eff} = p + \frac{2 \cdot \gamma_s}{r}, \qquad r = R \left(\frac{1-D}{6}\right)^{1/3} \tag{6.6}$$

6.2 Densifying mechanisms

If specific densifying mechanisms are known, the generalized equations given above can be further refined, as shown below.

6.2.1 Yielding

If the pressure at the contact between the particles is high enough to cause plastic flow, densification occurs rapidly (assumed to be instantaneous) until the contact areas between the particles are big enough so that the yield stress, σ_y is no longer exceeded. In the initial stage, the external pressure above which yielding occurs is given by:

$$p_{lim} = \frac{3\sigma_y}{4\pi R^2} \cdot a \cdot Z \cdot D, \quad D \leq 0.9 \tag{6.7}$$

An analogous analysis for the final stage leads to:

$$p_{lim} = \frac{2\sigma_y}{3} \cdot \ln\left(\frac{1}{1-D}\right), \qquad D > 0.9 \tag{6.8}$$

6.2.2 Creep

Creep is the permanent deformation of a material at a stress lower than the yield stress. The deformation occurs much slower than is the case of plastic deformation. When the applied stress is not high enough to cause plastic flow, deformation and densification can be caused by creep.

The linear shrinkage of a particle indented by a circular punch of area πx^2 is given by:

$$\dot{y} = \frac{9.\pi}{16} \cdot x \cdot C \cdot \left(\frac{p_1^{eff}}{3}\right)^n \tag{6.9}$$

where x is the contact radius and C and n are material constants in the constitutive law for creep, relating stain rate to stress:

$$\dot{\varepsilon} = C \cdot \sigma^n \tag{6.10}$$

This is the most general equation describing creep. In reality, several forms of creep are possible: deformation involving the motion of dislocation within the crystal lattice (dislocation creep), deformation accommodated by diffusion of the atoms through the crystal lattice (Nabarro-Herring creep), and deformation accommodated by diffusion of the atoms along the grain boundaries to elongate the grains along the stress axis (Coble creep).

In this study, only Coble creep is considered. Indeed, the dislocation density in NPs is very low [23], so dislocation creep can be ignored. We can also assume that Nabarro-Herring creep is negligible compared to Coble creep, since the grain

boundary density is much higher in nanomaterials, offering more diffusion paths for Coble creep to occur. The constitutive law for Coble creep is used [13]:

$$\dot{\varepsilon} = \frac{20 \cdot \sigma \cdot \pi \cdot \delta_{gb} D_{gb}}{k \cdot T \cdot d^3} \tag{6.11}$$

where d is the grain size and appropriate material constants for silver are listed in Table 6.1.

Table 6.1: Diffusion constants for silver

Melting Temperature, T_m (K)	962
Surface energy, γ_s (J/m^2) [15]	1.12
Grain boundary width, δ_{gb} (nm)	0.58
Surface width, δ_s (nm)	0.3
Atomic Volume, Ω (m^3)	1.71×10^{-29}
Density, ρ (kg/m^3)	10500
$D_{0,s}$ surface diffusion (m^2/s)[16,17,18]	1.33×10^{-12}
Q_s surface diffusion (J/mol)[16,17,18]	12.4
$D_{0,gb}$ grain boundary diffusion (m^2/s)[19,20]	1.29×10^{-7}
Q_{gb} grain boundary diffusion (kJ/mol)[19]	93
$D_{0,v}$, lattice diffusion (m^2/s)[19]	1.49×10^{-8}
Q_v lattice diffusion (J/mol)[19]	196.6
Diffusivity at temperature T (m^2/s) ('i' stands for s, gb or v)	$D_i = D_{0,i} \times e^{-Q_i/RT}$

Combining equations (6.1), (6.4) and (6.11) leads to the following densification rate during the initial stage:

$$\dot{D} = 5.3(D^2 \cdot D_0)^{1/3} \cdot \frac{x}{R} \cdot C \cdot \frac{p_1^{eff}}{3}, \quad D \leq 0.9 \tag{6.12}$$

During the final stage, equation (6.6) is used and the densification rate is given by:

$$\dot{D} = \frac{9}{4}(1 - D) \cdot C \cdot p_2^{eff}, \quad D > 0.9 \tag{6.13}$$

6.2.3 Pressure-assisted sintering

Sintering is the densification of powder compacts to create dense materials. It occurs when matter is transported by diffusion to the surface of the sintering neck (contact between two particles) by lattice diffusion or grain boundary diffusion, and is driven by a difference in chemical potential. The equations describing pressure-less sintering can be adapted to take into account the applied pressure.

In this analysis, the total flux of atoms diffusing through the lattice is several orders of magnitude smaller than the flux of atoms diffusing through grain boundaries, because of the very high density of grain boundaries due the nanocrystalline nature of the material. Therefore only grain boundary diffusion is considered. When the volume of mass transported by diffusion is equated to the volume change occurring during densification (see section 6.1) the densification rate during the first stage is:

$$\dot{D} = \frac{12 \cdot D^2}{D_0 \cdot R^3 \cdot g(D)} \frac{\delta_{gb} \cdot D_{gb}}{k \cdot T} \cdot \Omega \cdot Z \cdot p_1^{eff} \tag{6.14}$$

where g(D) is a geometric term given in [12], depending on D, D_0 and Z_0 and is in the range]0,3], and adequate silver diffusion data are given in Table 6.3

During the final stage, the analogous expression is given by:

$$\dot{D} = 54\frac{\delta D_b}{kTR^3}\cdot\Omega\cdot\left\{\frac{1-(1-D)^{2/3}}{3(1-D)^{2/3}-[1+(1-D)^{2/3}]\ln(1-D)-3}\right\}\cdot p_2^{eff} \quad (6.15)$$

6.2.4 Comparison between creep and pressure assisted sintering

In this study, creep densification and pressure-assisted sintering (densification by diffusion) are treated separately to follow the methodology presented by Ashby [12]. However, in the particular case of nano-Ag, we assumed that the physical mechanism leading to densification is grain boundary diffusion for both cases, (see previous sections). Thus, we should expect the densification rate to be comparable when calculating it with both methods. The calculations show that this is not the case. Indeed, the densification rate by creep is smaller by several orders of magnitudes. It is believed that the calculation of the densification rate is more accurate using the pressure-assisted sintering equation, rather that the densification by creep. One of the assumptions made in the densification by creep regime is that we can use the constitutive law for Coble creep (6.11) in the case of porous materials. In reality, this equation has been developed for fully dense materials: The atoms diffuse from a grain boundary under compressive stress ("source") to a grain boundary under tensile stress ("sink") to flatten the grains along the applied stress axis. In a porous material undergoing compressive stress, the sinks are open pores, and thus the creep equations should be adapter accordingly, which has not been done. Also, the grain boundary length is bigger in a fully dense material

(comparable to the grain size) than in a powder compact, especially during the initial stages of sintering where the contact between particles (the ‘necks’) are small. Therefore, diffusion distances are overestimated in equation (6.12), and the densification rate is underestimated. Thus, it is believed that that the densification by pressure-assisted sintering equation (6.14) describes better the densification process than the creep equation (6.12)

6.3 Mechanism map

6.3.1 Construction of the map

A plot showing the final density of porous nano-silver after compression under various loads can be constructed based on the theory presented in this chapter. In addition, for each particular density and applied stress, the dominant mechanism leading to deformation can be determined. The resulting plot is thus called a mechanism map. In this work, a mechanism map has been computed showing the dominant mechanisms leading to densification for all densities from the initial density (D_0=0.64) to full density (1) for a range of applied stress (0.001 to 10 times the yield stress of nano-Ag), at a temperature of 150°C.

The critical stress to initiate yielding of the material has been calculated for any density between the initial density and full density, using Equations (6.7) and (6.1). The region of densification by yielding lies below this boundary (Figure 6.1). The numerical computations were made using Octave software (version 3.2,4). The code necessary for the analysis is provided in appendix.

The densification rates for each potential densifying mechanism have been computed numerically with Octave by using the densification rate equations (6.11) to (6.14).These calculations showed that, outside of the yielding region (large applied stresses), the densification by pressure-assisted sintering occurs. The densification rate

for pressure-assisted sintering was higher than the calculated densification rate for Coble creep in all cases.

For more clarity, the applied stress is normalized with regard to the compressive yield strength. Zhang [11] evaluated the compressive yield strength of fully dense silver with a grain size of 50 nm to 390 ± 10 MPa at room temperature. Since it is the closest data available, it was used to compute the densification map in this work. We have assumed that the yield strength does not vary with temperature.

6.3.2 Discussion and comparison with experimental data

A densification map for nanostructured silver has been constructed and the experimentally determined densification data presented in chapter 5 have been overlaid on the map for comparison with the model predictions. At densities close to D_0, densification by yielding occurs even at very low applied stresses. This is because the contact region between the particles (initially spheres) is very small so the stress at the contacts is high enough to allow yielding, even at small loads. At larger applied stresses, the yielding regime occurs first, as expected. At a given applied stress, the region of the material located below the indenting punch densifies instantaneously by yielding until the contact areas between particles is large enough to drop the stress at the contacts below the stress required for yielding. Then, densification becomes time dependent and is governed by diffusion.

Figure 6.1: Mechanism map for the densification of nanostructured silver at 150°C

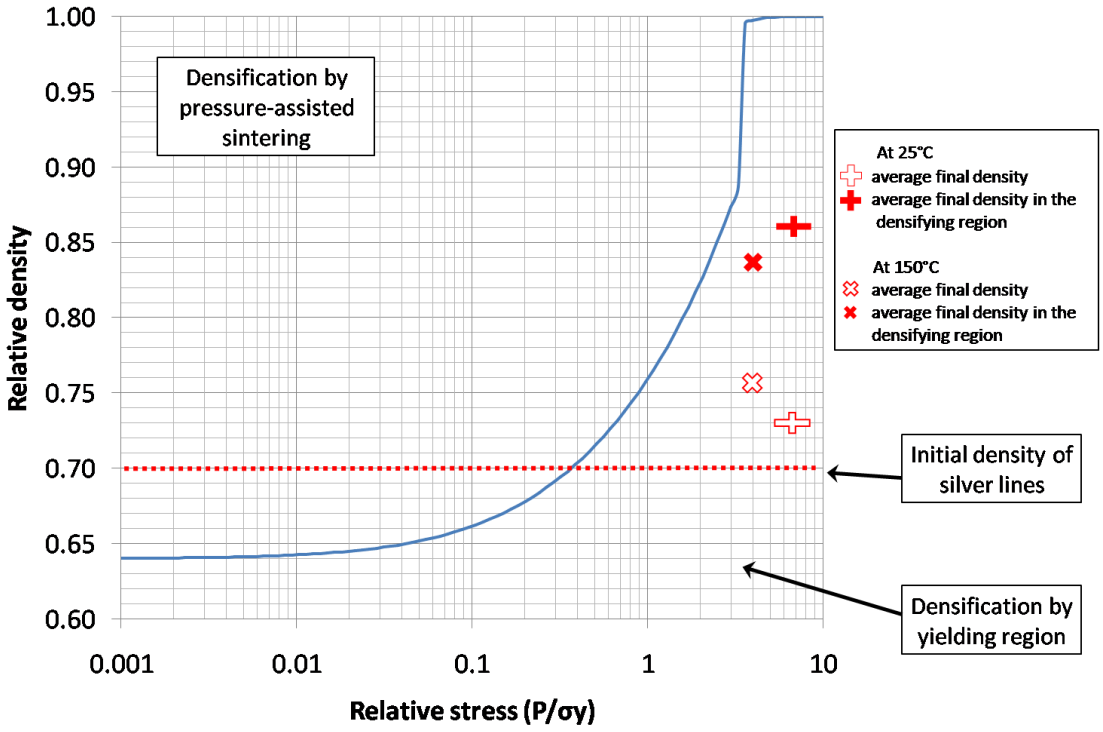

The experimental data plotted on Figure 6.1 correspond to the experiments presented on Figures 5.6 (at 25°C) and 5.10 (at 150°C). The average final relative density calculation is explained in section 5.2.1 and the final density in the densifying region (the region located just below the indenting punch) is explained in section 5.2.2.The analysis of the final density in the densifying region gives a more accurate view of the densification process than does the average final density, but it is still an underestimate of the actual density. As has been previously discussed (Figure 5.14), the density is likely much higher locally (at the center of the line), and it may approach 100% as discussed for

the experiment at 150°C. However, this is not reflected in the experimental data presented on the densification map because it is difficult to quantify.

These results show the importance of accurately determining the local density of the line during the compression experiment and in knowing the yield strength of the materials. For example, the densification map predicts that for the conditions at which both experiments were conducted, only plasticity should be observed (i.e. there should not be any time-dependent deformation, since the data points lie to the right of the line in Figure 6.1). However, the experiments in Chapter 5 clearly showed significant time-dependent deformation behavior, particularly at 150˚C. As was discussed previously, it is probable that there is some temperature dependence to the yield strength, which was not considered in the map and which would tend to shift the blue in Fig. 6.1 to the right. Thus, it would be more likely that under the experimental conditions that were used, some time dependent deformation would be predicted. In addition, it is apparent from Fig. 6.1 that if the actual local density is higher than the final average density in the densifying region as we expect, this would also tend to move the experimental data closer to the transition regime where time-dependent deformation is predicted.

One suggestion for improving the assessment of time-dependent plasticity is to perform a finite element analysis which would help to assess the complex geometries involved in this problem. The experiments conducted under rapid deformation conditions could be performed first and compared to a finite element analysis where only plasticity is considered. Good correlations between the predicted and experimental deformations

strains would allow the yield strength of the material to be determined accurately. The experiments then be repeated at longer times and the simulations run with both plasticity and time-dependent strains to extract the time dependent material properties and the local densities. Unfortunately, this analysis is beyond the scope of this thesis.

7. Conclusions

Nanocrystalline silver films have been produced by combining the LAMA process to produce an aerosol of nanoparticles with a direct-writing setup to accelerate the NPs and impact them on a translating substrate. The two main points discussed in this work are the mechanisms governing the film deposition and the mechanical properties of the produced films.

The new experimental data is discussed in the context of existing literature in the field of cluster deposition onto a substrate. Many computer simulation studies have been published in this area, because it is a promising technique to deposit epitaxial coatings at conditions that are gentle to the substrate. The film densities and morphologies were in qualitative agreement with computer simulations available in the literature, as well as the prediction that the collection efficiency of nanoparticles can be improved by raising the substrate temperature. In addition, the experiments revealed that the choice of the impacting substrate influences the collection efficiency. We observed that silver nanoparticles were more likely to stick on a metallic layer than on an oxide layer. The influence of impacting substrate had not been investigated so far to our knowledge, either experimentally or by computer simulation. Also, it has been observed that the deposition efficiency increases when raising the substrate temperature.

Unfortunately, whether the nanoparticles crystal lattice aligns with the substrate upon impaction (a process called “epitaxial deposition”), as predicted by computer simulations at the involved impaction speed, remains an open question. A possible way to

answer to this question is to observe the cross section of a deposited film with a TEM to determine the crystallographic orientation of the grains within the film. Although an appropriate procedure to prepare cross-section TEM samples was identified and the preparation process was started, TEM observations were not carried out in the scope of this thesis.

Compression experiments were conducted on the produced films, varying the temperature and the loading time. The films are made of porous nanostructured silver produced by LAMA. Local densification of the films was observed and quantified. Both temperature and loading time were shown to have a significant influence on deformation. An increase in the densification that occurred during compression has been observed when the process temperature was raised from room temperature to 150°C. The loading time also has a big influence on the final strain at 150°C, which reveals the presence of a time-dependent deformation process.

A viable process to create seals for microelectromechanical systems (MEMS) using nano-silver lines has been proposed. MEMS packaging remains a key challenge since it can represent up to 90% of the total cost [21]. Also, lower processing temperature is desirable to enable the use of new materials. The proposed process consists of writing a square of lines around the device and subsequently compress and bond the top of the lines to a second substrate at low temperatures to create a seal.

Finally, to understand the mechanisms involved in densification of porous nanostructured silver, experimental data were compared to a densification model. In this

model, two main mechanisms govern densification (1) densification by yielding at high applied stresses and low densities and (2) densification by diffusion (which is time-dependent). The experimental data did not match the predictions of the model mainly because the densification is highly non-uniform within the compressed line and the density could not be precisely determined at every location. To overcome these difficulties, finite element analysis would be useful to take into account the variations in local density and quantify the contribution of both mechanisms leading to densification, yielding and time-dependent deformation.

Appendix

The following Octave code has been used for modeling the densification process of porous nanostructured silver. The calculations are based on a model proposed by Ashby [12] that has been adapted to nano-silver. The different codes that have been used in this work are as follows:

1) Function calculating the density at which plastic deformation stops, as a function of applied compressive stress.
2) Octave script (m file) intended to plot a densification map. This gives the dominant mechanism governing densification depending on the applied compressive stress (X-axis) and density (Y axis).
3) Function calculating the densification rate assuming it is governed by diffusional creep.
4) Function calculating the densification rate assuming it is governed by pressure assisted sintering. Calculations show that the densification rate in 4 is always greater than in 4.

1) This function calculates the density at which plastic deformation stops, as a function of applied stress. Plastic deformation occurs as long as the effective stress at the particles contacts exceeds the yield stress.

```
# Dmax_yield.m
# x->(P/sigma_y)
# x varies in the range [.001,10]
# y-> Final Density when yielding stops


function y=Dmax_yield(x)

#constants
    #initial density of a random packed body
    D0=0.64;

# first stage(D<0.9)
    y1= D0 - 1/20 .+ ((9+30.*x.*pi).^(0.5))./60;

#second stage (D>0.9)
```

```
    y2=(exp(1.5.*x)-1)./(exp(1.5.*x));

if(y1<0.9)
    y=y1;
    else y=y2;
endif

endfunction
```

2) This .m file is intended to plot a densification map. This gives the dominant mechanism governing densification depending on the applied compressive stress (X-axis) and density (Y axis).

```
# draws the densification map @ 150C
# x -> P/(yield stress)
# y -> Density at which the densification by yielding stops
# no other boundary is necessary since the densification rate by
#diffusion is always greater than the densification rate by creep

N=100 # number of estimations

# creates the vectors for x and y axis
x=logspace(-3,1,N);
y=zeros(1,N);

for k=1:N y(k)=Dmax_yield(x(k));
endfor

#plot the data
semilogx(x,y_smooth,'r-')
axis([0,1,0.6,1]);axis "autox";
title('Densification map for nano-silver',"fontsize",18)
xlabel('P/\sigma_y',"fontsize",18)
ylabel("Relative density","fontsize",18)

# write the data in an output file
#z = [x', y'];
#save -ascii ``output_file.txt'' z;
```

3) This function calculates the densification rate assuming it is governed by diffusional creep.

```
#D2_rate.m
#function that returns the densification rate in the creep regime
#  as  a  function  of  relative  density  and  relative  applied
#stress(applied stress)/(yield stress)
# at a given temperature
```

```
function y=D2_rate(D,p)

# constants
    # Initial density
    D0=0.64;
    # initial particle radius, m
    R = 2.5e-9;
    # Temperature, K
    T = 273+150;
    #Gas constant, m2 kg s-2 K-1 mol-1
    r=8.314472;
    # material constants
        # Atomic volume, m3
        Omega=1.71e-29;
        # lattice diffusion, m2/s
        Dv=(1.49e-8)*exp(-196600/(r*T));
        # grain grain boundary diffusion, m3/s
        deltaDb=0.58e-9*(1.27e-7)*exp(-93000/(r*T));
    #Boltzman constant, m^2 kg s-2 K-1
    k=1.3806503e-23;
    # NH and Coble creep constants:

crp_cst=(20*Omega*Dv*(1+pi*deltaDb/(2*R*Dv)))/(k*T*(2*R)^2);
        n=1;
    #surface tension, J/m^2
    gamma = 1.12;
    #contact radius, m
    x = (D-D0).^(1/2).*R;

    #effective pressure at contacts, Pa
    p1_star     =     (4.*pi*p)./((D-D0).*(160.*(D-D0)+16))     +
gamma.*(2.8.*(R-    x)./x.^2-1./x);#neglect p_i
    p2_star = p+(2*gamma*(6/(1-D))^(1/3)/R); #neglect p_i

# calculation of D2_rate
    # initial stage
    if(D<0.9)

y=5.3.*(D.^2*D0).^(1/3).*(x./R).*(crp_cst).*(1/3).*p1_star.^n;
    #final stage
    else
        y=1.5*crp_cst.*D.*(1-D).*(1.5*p2_star/n)^n./(1-(1-
D)^(1/n))^n;
    endif
```

4) This function calculates the densification rate assuming it is governed by pressure assisted sintering

```
#D3_rate
#function that returns the densification rate in the sintering
regime
```

```
# as a function of relative density and relative applied
#stress:(applied stress)/(yield stress)
# at a given temperature

function y=D3_rate(D,p)

# constants
    # Initial density
        D0=0.64;
    # initial particle radius, m
        R = 2.5e-9;
    # Temperature, K
        T = 273+150 ;
    #surface energy, J/m^2
        gamma = 1.12;
    #neck radius, m
        X = (D-D0).^(1/2).*R;
    #effective pressure at contacts, Pa
        p1_star    =    (4.*pi.*p)./((D-D0).*(160.*(D-D0)+16))    +
gamma.*(2.*(R-X)./(X.^2)-1./X);
        p2_star = p+(2*gamma*(6/(1-D)).^(1/3)./R);
    #Gas constant, m2 kg s-2 K-1 mol-1
        r=8.314472;
    # material constants
        # Atomic volume, m3
            Omega=1.71e-29;
        # lattice diffusion, m2/s
            Dv=(1.49e-8)*exp(-196600/(r*T));
        # grain grain boundary diffusion, m3/s
            deltaDb=0.58e-9*(1.27e-7)*exp(-93000/(r*T));
    #density, kg/m^3
        rho=10500;
    #number of contacts per particle
    Z=7.3+15.5.*((D/D0).^(1/3)-1);
    #Boltzman constant, m^2 kg s-2 K-1
    k=1.3806503e-23;

# geometric factor
    g=((D./D0).^(2/3)-1).*(7.3+3.875*((D./D0).^(2/3)-1));

# calculation of densification rate in the diffusion regime,
D3_rate:

if(D<0.9)
    # initial stage
    y=
(12*D.^2*(deltaDb+rho*Dv).*Omega.*Z.*p1_star)./(D0.*R^3*g.*k.*T);
else
    #final stage
    y=                          (54.*Omega.*(deltaDb+rho*Dv).*(1-(1-
D).^(2/3))*p2_star)./(k*T*R^3.*(3*(1-D)^(2/3)-(1+(1-
D)^(2/3)).*log(1-D)-3));
endif
```

References

[1] K. Gleason, “Engineering Nanocomposite Polymer Membranes for Olefin/Paraffin Separation”, Dissertation, The University of Texas at Austin (2011)

[2] W. T. Nichols, "Production and controlled collection of nanoparticles toward manufacturing of nanostructured materials," Ph.D. dissertation, The University of Texas, Austin, TX, (2002)

[3] C. Huang, W.T. Nichols,D.T. O’Brien, M.F. Becker,D. Kovar et al. (2007) Supersonic jet deposition of silver nanoparticle aerosols: Correlations of impact conditions and film morphologies, J. Appl. Phys. 101, 064902 (2007)

[4] I. F. Gallardo, "Tuning of core-shell heterostructured nanoparticles generated by laser ablation of microparticles" Ph.D. dissertation, Department of Physics, University of Texas at Austin (2009)

[5] K. Nordlund, T.T. Järvi, K. Meinander, J. Samela, Cluster ion–solid interactions from meV to MeV energies, Appl. Phys. A 91, 561–566 (2008)

[6] H. Haberland, Z. Insepov, M. Moseler, Molecular-dynamics simulation of thin-film growth by energetic cluster impact, Physical Review B (1995)

[7] K. Meinander, K. Nordlund, J. Keinonen, Size dependant epitaxial cluster deposition: The effect of deposition energy, Nuclear Instruments and Methods in Physics Research B 242, 161-163 (2006)

[8] K. Meinander, K. Nordlund, Irradiation-induced densification of cluster-assembled thin films, Physical review B 79, 045411 (2009)

[9] A. Albert, “Nanostructured Ag produced by LAMA”, Dissertation, The University of Texas at Austin (2007)

[10] M. Nahar, “Highly Conductive, Nanoparticulate Thick Films Processed at Low Processing Temperatures”, Dissertation, The University of Texas at Austin (2012

[11] L. Zhang, Fabrication of bulk nanostructured silver material from nanopowders using shockwave consolidation technique, Materials Science and Engineering A 487 219-227 (2008)

[12] M.F Ashby, Practical Applications of Hot Isostatic Pressing Diagrams: Four Case Studies, Metallurgical Transactions A, vol. 14A, 211-221 (1983)

[13] T.H Courtney, Mechanical behavior of materials, McGraw-Hill, (2000)

[14] M.F Ashby, Boundary defects and atomistic aspects of boundary sliding and diffusional creep, Surface Science 31 498-542 (1972)

[15] H. Jones, The Surface Energy of Solid Metals, Met. Sci. J., 5 15-18 (1971)

[16] A.G. Guy, Essentials of Materials Science. McGraw-Hill, New York, (1976)

[17] J.M. Blakely and H. Mykura, Surface Self Diffusion and Surface Energy Measurements on Platinum by the Multiple Scratch Method, Acta Metall., 10 [5] 565-572

[18] H. Göbel and P. von Blanckenhagen, A Study of Surface Diffusion on Gold with an Atomic Force Microscope, Surf. Sci., 331-333 [Part 2] 885-890 (1995)

[19] N.L. Peterson, Grain-boundary diffusion in metals, International Metals Reviews, 28 [2] 65-91 (1983)

[20] M. DiBattista and J.W. Schwank, Determination of Diffusion in PolycrystallinePlatinum Thin Films, J. Appl. Phys., 86 [9] 4902-4907 (1999)

[21] T. Srinvasan, Wafer-to-Wafer Bonding, Lecture 25, available online: http://www-bsac.eecs.berkeley.edu

[22] M. Nahar *et al.* Metal-on-oxide nanoparticles produced using laser ablation of microparticle aerosols, Journal of Nanoparticle Research (2011)

[23] C. Carlton , Dislocation instability in nanoscale particles, Materials Research Society Symposium Proceedings, v 903, p 85-90, Amorphous and Nanocrystalline Metals for Structural Applications (2005)

[24] B. T. Chen and H. C. Yeh, An improved virtual impactor: Design and performance, Journal of Aerosol Science, vol. 18, pp. 203-214, (1987)

[25] J. F. de la Mora, *et al.*, Hypersonic impaction of ultrafine particles, Journal of Aerosol Science, vol. 21, pp. 169-187, (1990)

[26] Liwei Lin, Berkeley Sensor and Actuator Center, University of California at Berkeley, lecture on Packaging issues of MEMS devices, available online: www.seas.ucla.edu/ethinfilm/Pb-freeWorkshop/pdf/lin.pdf

[27] M.N. Rahaman, Ceramic processing and sintering, 1995, Marcel Drekker, Inc., New York, pg 23; pg 387 (1995)

[28] V. A. Marple and C. M. Chien, Virtual Impactors: A Theoretical Study, Environmental Science & Technology, vol. 14, pp. 976-985, (1980)

[29] Nichols et al., Gas and pressure dependence for the mean size of nanoparticles produced by laser ablation of flowing aerosols, Journal of Nanoparticle Research 2: 141–145 (2000)

[30] Online electron microscopy courses, http://www.emcourses.com/sputter.htm

Vita

Guillaume Noiseau was born in Sainte-Adresse, France, in 1988. He graduated with highest honors from Lycée J-F. Millet High School in Cherbourg, France in 2005 and then enrolled in Classes Préparatoires aux Grandes Ecoles-CPGE at Lycée Victor Grignard, also in Cherbourg. Here, Guillaume undertook a three year intense undergraduate preparation for the national entrance examinations for French engineering universities. Following those examinations, he was admitted at Ecole Centrale de Lille in 2008 for general engineering studies. He enrolled at the University of Texas at Austin in 2010 to pursue a Master of Science degree in Materials Science and Engineering under the supervision of Dr Desiderio Kovar.

Permanent e-mail adresses: guillaume.noiseau@gmail.com or gnoiseau@utexas.edu

This thesis was typed by the author.